JOURNAL OF PETROLOGY | VOLUME 47 | NUMBER 10 | PAGES 2021–2046 | 2006 | doi:10.1093/petrology/egl035

Evolution of a Porphyry-Cu Mineralized Magma System at Santa Rita, New Mexico (USA)

A. AUDÉTAT[1]* AND T. PETTKE[2†]

[1]BAYERISCHES GEOINSTITUT, UNIVERSITÄT BAYREUTH, 95440 BAYREUTH, GERMANY

[2]INSTITUTE OF ISOTOPE GEOCHEMISTRY AND MINERAL RESOURCES, ETH ZENTRUM NO, 8092 ZÜRICH, SWITZERLAND

RECEIVED JUNE 30, 2005; ACCEPTED JUNE 12, 2006; ADVANCE ACCESS PUBLICATION SEPTEMBER 7, 2006

The magmatic processes leading to porphyry-Cu mineralization at Santa Rita are reconstructed on the basis of petrographic studies, thermobarometry, and laser-ablation inductively-coupled-plasma mass-spectrometry analyses of silicate melt and sulfide inclusions from dikes ranging from basaltic andesite to rhyodacite. Combined results suggest that magma evolution at Santa Rita is similar to that of sulfur-rich volcanoes situated above subduction zones, being characterized by repeated injection of hot, mafic magma into an anhydrite-bearing magma chamber of rhyodacitic composition. The most mafic end-member identified at Santa Rita is a shoshonitic basaltic andesite that crystallized at 1000–1050°C, 1–3 kbar and log f_{O_2} *= NNO + 0·7 to NNO + 1·0, whereas the rhyodacite crystallized at 730–760°C and log* f_{O_2} *= NNO + 1·3 to NNO + 1·9. Mixing between the two magmas caused precipitation of 0·1–0·2 wt % magmatic sulfides and an associated decrease in the Cu content of the silicate melt from 300–500 ppm to less than 20 ppm. Quantitative modeling suggests that temporal storage of ore-metals in magmatic sulfides does not significantly enhance the amount of copper ultimately available to ore-forming hydrothermal fluids. Magmatic sulfides are therefore not vital to the formation of porphyry-Cu deposits, unless a mechanism is required that holds back ore-forming metals until late in the evolution of the volcanic–plutonic system.*

KEY WORDS: *porphyry-Cu; sulfur; sulfides; magma mixing; LA-ICP-MS*

INTRODUCTION

Porphyry-copper deposits represent large geochemical anomalies of sulfur and copper. It is now widely accepted that both of these elements originate from underlying magmas and are transported to the site of mineralization by aqueous fluids (Evans, 1993; Hedenquist & Lowenstern, 1994; Bodnar, 1995). Although the principles leading to porphyry-Cu mineralization are fairly well understood, it is not clear what role sulfur plays in the overall metal-enrichment process. Copper may be linked to sulfur by: (1) partial melting of a Cu- and S-rich source; (2) coupled assimilation of Cu and S during magma ascent and storage; (3) formation (and later destruction) of magmatic sulfides or immiscible sulfide melts during magma crystallization; or (4) simultaneous partitioning of S and Cu into exsolving aqueous fluids. Knowledge of the relative importance of these processes requires a quantitative understanding of the evolution of Cu and S in porphyry-Cu systems.

The main aim of this paper is to present a detailed reconstruction of the magmas associated with porphyry-Cu mineralization at Santa Rita, with particular focus on the behavior of S and chalcophile elements. Much of the chemical information used in this study stems from laser-ablation inductively coupled plasma mass spectrometry (LA-ICP-MS) analyses of crystallized silicate melt inclusions, which represent small droplets of silicate melt trapped in minerals at specific stages of magma evolution (e.g. Lowenstern, 1995). Melt inclusions are particularly helpful if original concentrations of volatile elements such as S and Cu are to be quantified, because bulk-rocks are depleted (or, in the case of mineralization, enriched) in these elements to *a priori* unpredictable

*Corresponding author. E-mail: andreas.audetat@uni-bayreuth.de
†Present address: Institut für Geologie, Baltzerstrasse 1+3, Universität Bern, 3012 Bern, Switzerland.

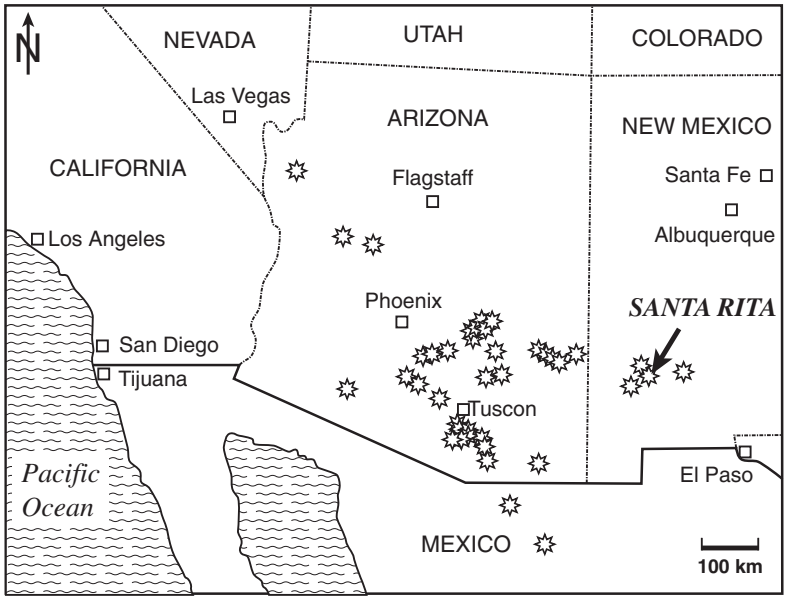

Fig. 1. Location of Santa Rita (Chino Mine) and other porphyry-Cu deposits (stars) in the southwestern USA (after Titley & Anthony, 1989).

degrees. Together with petrographic observations and chemical analyses of host minerals and sulfide inclusions, the melt inclusion data are used to develop quantitative crystallization models that allow the role of magmatic sulfides in the mineralization process to be investigated.

GEOLOGICAL SETTING

The porphyry-copper deposit at Santa Rita (Chino Mine) in southwestern New Mexico belongs to a suite of ~50 similar deposits that formed in the American Southwest during the Laramide orogeny (~45–75 Ma) as a result of plate subduction along an Andean-type continental margin (Fig. 1). The deposits occur in a belt located about 350–450 km landward of the reconstructed continental margin and show a close spatial and temporal association with andesitic to dacitic, calc-alkaline volcanism (Titley, 1993). Because Santa Rita is situated far inland, it is one of the youngest and therefore least eroded occurrences of this suite, and it has been little affected by Basin-and-Range tectonics.

An excellent summary of the geology of Santa Rita has been given by Rose & Baltosser (1966), whereas detailed geological and petrographic descriptions have been given by Jones *et al.* (1967). Igneous activity in the region began in the Late Cretaceous with the intrusion of dioritic to quartz-dioritic sills into a Precambrian basement that was covered by an ~1 km thick sequence of Paleozoic and Mesozoic sediments. Subsequently, basaltic–andesitic to andesitic magma erupted on the surface and formed mafic dikes and an intrusive body at depth, with both volcanic and intrusive rocks being exposed at the present level of erosion. This event was followed by intrusion of granodioritic to quartz-monzodioritic magma in the form of stocks (Santa Rita and Hanover–Fierro) and genetically related dikes. The last stage of magmatic activity is represented by dikes of rhyodacitic to rhyolitic composition, which cut across all other lithologies (Fig. 2). Most of the Cu-mineralization occurred between the intrusion of the quartz-monzodioritic magma and the formation of the rhyodacite dikes (Jones et al., 1967). Between 1911 and 1966, about 250 Megatons of ore with an average content of 0·8–0·9 wt % Cu were extracted from Santa Rita (Rose & Baltosser, 1966). The mine is at present operating at an ore grade of 0·2 wt % Cu and 0·02 wt % Mo (R. North, personal commununication, 2000).

METHODS

To constrain the magmatic processes leading to porphyry-Cu mineralization at Santa Rita we collected samples from dikes ranging from basaltic andesite to rhyodacite in composition. One specimen from an anhydrite-bearing quartz-monzodiorite porphyry dike (sample SR8) has been described in detail by Audétat *et al.* (2004). Because most rocks in the study area are partly altered we did not perform whole-rock analyses [an extensive dataset has been given by Jones *et al.* (1967)], but rather relied on melt inclusion data to reconstruct the magma evolution.

From each rock sample at least five polished sections of 100–300 μm thickness were prepared and examined with a standard petrographic microscope. Special attention

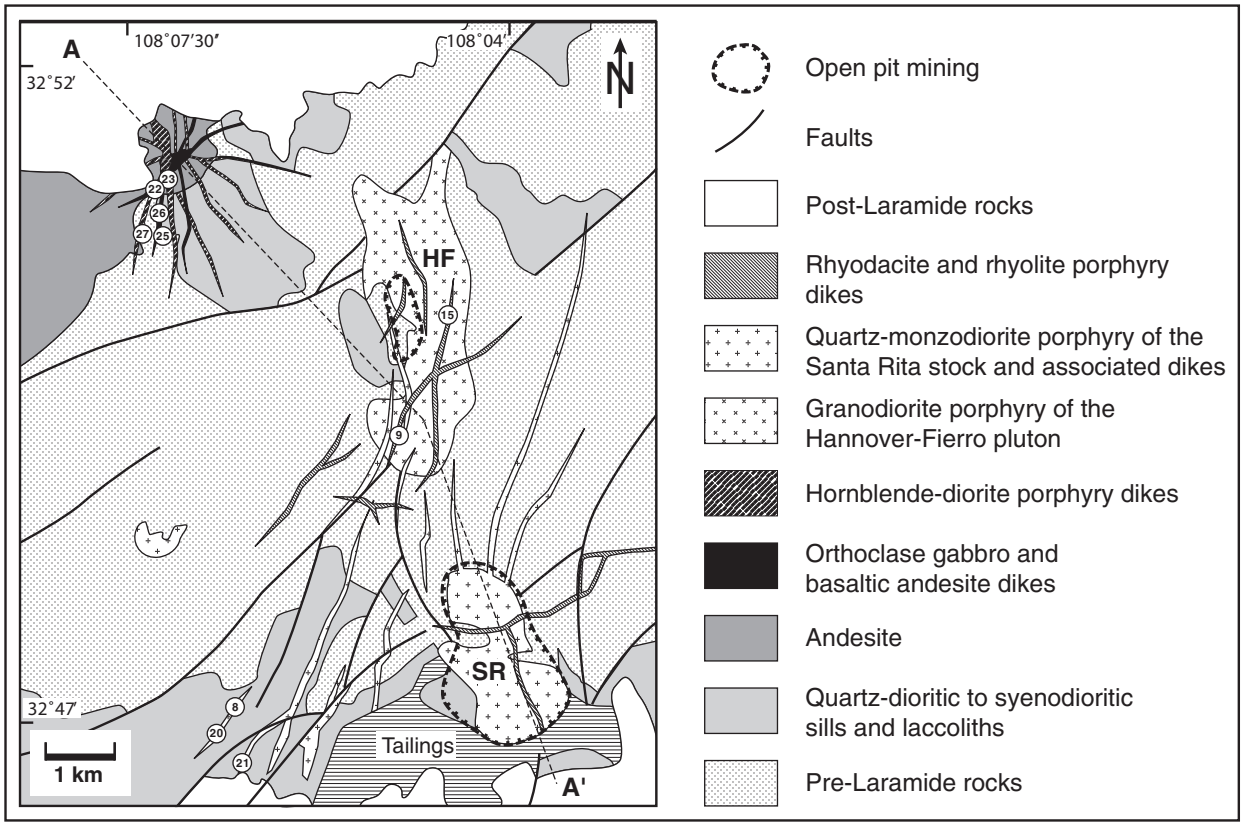

Fig. 2. Simplified geological map of the Santa Rita area, showing sample locations and major lithologies (after Hernon *et al.*, 1964). HF, Hannover–Fierro pluton; SR, Santa Rita Stock. Numbers in circles refer to the sample names used throughout the text (e.g. 22 corresponds to sample 'SR22'). Line A–A' marks the trace of the cross-section shown in Fig. 10.

was paid to the occurrence of melt and mineral inclusions within phenocrysts, as they provide valuable information about the phase assemblage at a given time. The study of mineral inclusions is particularly important for phases such as magmatic anhydrite or sulfides, which—if accessible to fluids—are destroyed after rock solidification. Mineral inclusions that could not be identified optically were identified by Raman spectroscopy, using a Dilor XY Raman microprobe with a resolution of 1800 lines per mm, a focal length of 500 mm, a Peltier-cooled CCD detector with 1024 elements, and reference spectra of known minerals.

Selected phenocrysts and enclosed mineral, melt or sulfide inclusions were analyzed by electron microprobe or LA-ICP-MS. For the former type of analysis, the inclusions were exposed to the surface by polishing. In the case of LA-ICP-MS, entire unexposed inclusions were drilled out of the host mineral by the laser beam. The strength of LA-ICP-MS lies in the fact that it allows inclusions to be analyzed that became heterogeneous after their entrapment and cannot be re-homogenized properly or quenched to a homogeneous phase (e.g. fluid inclusions, magmatic sulfides, crystallized silicate melt inclusions that lost volatiles). However, LA-ICP-MS has the disadvantage that it delivers relative element abundances only, which need to be transformed into absolute values by means of an internal standard (Longerich *et al.*, 1996; Günther *et al.*, 1998; Halter *et al.*, 2002*b*). Deconvolution of the mixed signals into contributions from host vs inclusion is relatively straightforward for chemically simple host minerals such as quartz, but becomes increasingly difficult for chemically complex minerals. Details of the quantification procedure and the validity of melt inclusion compositions in general are given in the Appendix. The LA-ICP-MS system used in this study is composed of a 193 nm Excimer Laser (Lambda Physik, Germany), special energy homogenization optics (Microlas, Germany), and an Elan 6100 quadrupole mass spectrometer (Perkin Elmer, Canada). Technical information about this method has been given by Günther *et al.* (1998) and Heinrich *et al.* (2003). Analytical conditions were very similar to those used in other melt inclusion studies (Pettke *et al.*, 2004).

Electron microprobe analyses were performed on a JEOL-Superprobe, using 15 kV acceleration voltage,

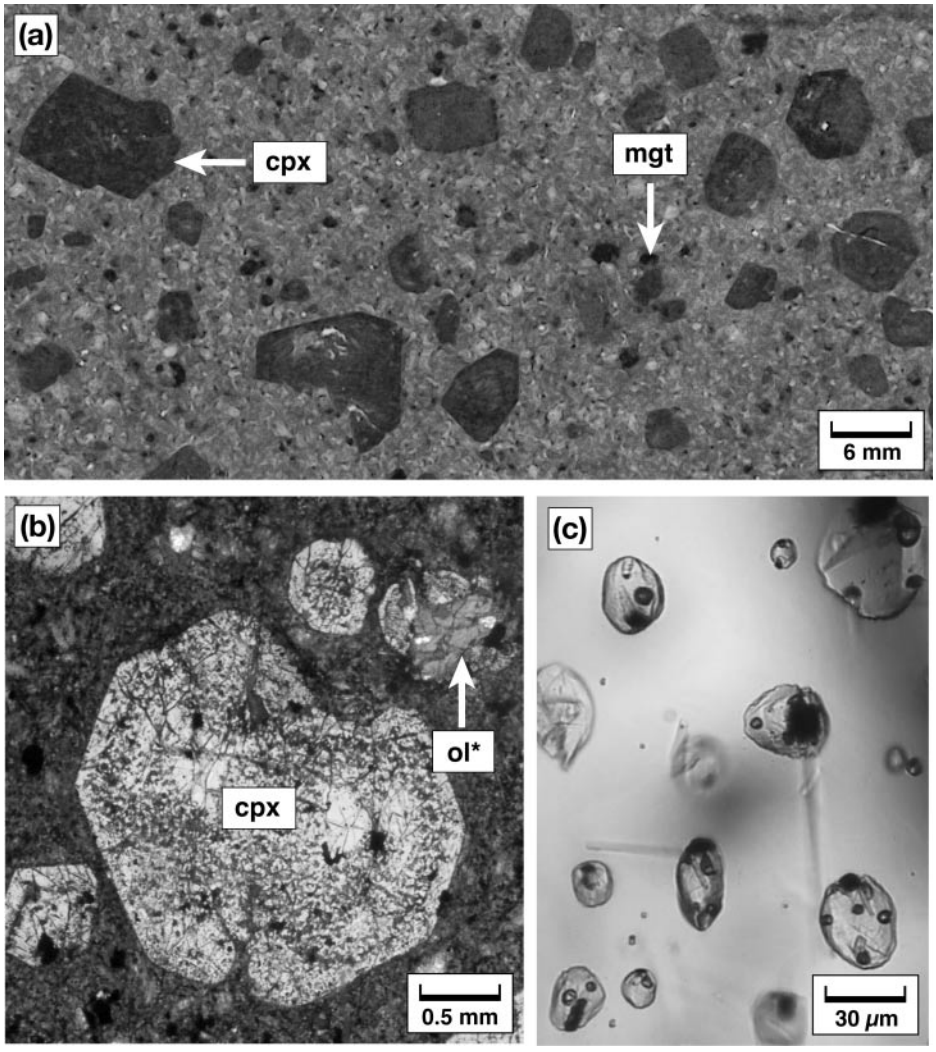

Fig. 3. Petrography of basaltic andesite sample SR26: (a) photograph of a polished surface; (b) photomicrograph of an augite phenocryst in a thick section (transmitted light); (c) partly crystallized melt inclusions in augite (transmitted light). ol*, altered olivine. (For other abbreviations, see Table 1.)

20 nA sample current, a fixed beam of 5 μm diameter, and peak counting times between 20 and 60 s. Elements were standardized on diopside, plagioclase, albite, sanidine, tausonite ($SrTiO_3$), rhodonite, almandine and wüstite.

MINERALOGY AND CHEMISTRY OF MAGMA TYPES

Basaltic andesite

Dikes of basaltic andesite in the northwestern corner of the investigated area (samples SR26 and SR22 in Fig. 2) appear dark green to dark gray on fresh surfaces and contain phenocrysts of augite (~20 vol. %; up to 8 mm diameter), magnetite (2–4 vol. %), olivine (3–5 vol. %; replaced by chlorite, carbonate and magnetite), and apatite (<1 vol. %) set in a fine-grained groundmass (Fig. 3a). Phenocrystic plagioclase is rare or even absent in sample SR26, but common in sample SR22 (~20 vol. %; up to 5 mm long; Table 1). Augite phenocrysts in sample SR26 contain numerous melt inclusions (Fig. 3b). Other inclusions present in the augite phenocrysts comprise apatite, magnetite, plagioclase (only in SR22; $An_{67–70}$), olivine ($Fo_{64–70}$) and rare magmatic sulfides. Most augite crystals are normally zoned from Mg-, Cr- and Ni-rich cores to Fe-rich rims, but two cases of inverse zonation have been observed as well.

LA-ICP-MS analyses of 25 melt inclusions in augite and apatite phenocrysts (Table 2) reveal melt compositions of 54–57 wt % SiO_2, 5–8 wt % FeO, and 3–6 wt % MgO. The remarkably high potassium content

Table 1: Petrography and inclusion assemblages of main magma types at Santa Rita

Phenocrysts	vol. %	Contains inclusions of:													
		ol	cpx	apa	sulf	plag	hbl	mgt	ilm	zirc	bio	tit	anhy	calc	alla
Basaltic andesite, sample SR26															
augite	20–30	×		×	×			×							
(olivine)*	3–5														
magnetite	2–4				×										
apatite	<1							×							
Basaltic andesite, sample SR22															
augite	20–25			×	×	×		×							
plagioclase	20–25		×					×							
(olivine)	2–4														
magnetite	2–4				×										
apatite	<1							×							
Hornblende-diorite, samples SR23, SR25, SR27															
plagioclase	20–30		×	×			×	×							
hornblende	10–15		×	×	×	×		×							
augite/biotite	3–6			×	×	×	×	×							
magnetite	2–3				×										
apatite	<1				×			×							
Quartz-monzodiorite, samples SR8, SR20, SR21															
plagioclase	15–25			×			×	×							
hornblende	3–7	×	×	×	×	×		×				×			
(biotite)	3–7														
(augite/olivine)	2–4														
quartz	2–4			×		×	×	×		×	×	×		×	×
(anhydrite)	1–2			×											
(Kfsp)	<1														
titanite	<1			×		×		×	×	×					
magnetite	<1														
apatite	<1					×	×	×			×	×	×		
Rhyodacite, samples SR9, SR15															
plagioclase	20–40			×			×	×			×	×	×		
hornblende	3–10			×	×	×		×			×		×		
quartz	2–8			×		×	×	×		×	×	×			×
(biotite)	1–5														
K-feldspar	1–3														
(anhydrite)	1–3			×											
titanite	<1			×					×						
magnetite	<1				×				×						
ilmenite	<1							×							
apatite	<1							×		×	×		×		

*Parentheses signify that this phenocryst phase was destroyed during subsolidus alteration.
ol, olivine; cpx, clinopyroxene; apa, apatite; sulf, sulfides; plag, plagioclase; hbl, hornblende; mgt, magnetite; ilm, ilmenite; zirc, zircon; bio, biotite; tit, titanite; anhy, anhydrite; calc, calcite; alla, allanite.

(4·7–7·6 wt % K_2O) identifies these melts as shoshonitic (Fig. 4). Their trace element signature is typical of subduction-related, mafic to intermediate magmas, showing high ratios of Th/La (0·20), Ba/La (40), Pb/Ce (0·25), La/Nb (3·5) and Th/Nb (0·8), and high contents of Cs (6 ppm), Rb (200 ppm), Ba (1000 ppm), Th (7 ppm), La (30 ppm), Ce (60 ppm), Pb (13 ppm) and Sr (700 ppm) relative to MORB (e.g. Kelemen

Table 2: Representative LA-ICP-MS analyses of melt inclusions

Sample name	Host	SiO_2	TiO_2	Al_2O_3	FeO	MnO	MgO	CaO	Na_2O	K_2O	P_2O_5	Sum	B
Basaltic andesite													
SR26MI2cpxArim 20 μm***	cpx	59·1	0·29	17·1	3·69	0·12	3·30	6·98	4·05	5·74	—	100	81
SR26MI3cpxArim 50 μm***	cpx	54·9	0·97	16·7	7·25	0·16	3·99	7·87	3·72	5·47	—	101	46
SR26MI3cpxAcore 20 μm***	cpx	54·9	0·96	16·5	7·73	0·15	4·46	7·86	3·35	5·01	—	101	(75)
SR26MI3cpxBcore 40 μm***	cpx	56·7	1·03	16·3	7·41	0·13	2·51	7·54	3·71	4·70	—	100	10
SR26MI1cpxBcore 40 μm**(*)	cpx	56·0	0·82	15·7	8·19	0·13	3·25	7·68	3·53	4·73	—	100	46
SR26MI1cpxCcore 30 μm***	cpx	56·0	0·62	15·7	8·34	0·17	2·84	7·68	3·90	4·79	—	100	44
SR26DcpxNMI3 30 μm***	cpx	52·6	1·05	17·9	7·93	0·18	3·89	8·32	3·11	5·31	0·71	100	45
SR26DcpxNMI2 30 μm***	cpx	52·6	1·17	18·3	6·62	0·15	5·30	8·59	2·83	4·98	0·52	101	35
SR26DcpxNMI1 30 μm***	cpx	54·2	0·93	17·4	7·11	0·17	4·65	7·83	3·03	5·01	0·52	100	42
SR26DcpxMMI1 30 μm***	cpx	55·5	0·77	17·4	5·85	0·16	4·63	7·58	3·17	5·23	0·44	100	53
SR26DcpxMMI4 30 μm***	cpx	56·5	0·62	16·9	5·57	0·13	4·44	6·93	3·39	5·57	0·43	100	83
SR26AcpxLMIrim 30 μm***	cpx	53·6	0·99	16·8	7·94	0·15	3·42	7·39	2·84	7·10	0·48	100	80
SR26AcpxLMImiddle 30 μm***	cpx	55·5	0·66	17·2	5·91	0·12	3·38	7·45	3·10	6·55	0·71	100	65
SR26AcpxLMI2core 60 μm***	cpx	56·9	0·89	16·9	7·97	0·16	—	6·73	4·08	6·38	0·80	100	56
SR26AcpxLMI1core 60 μm***	cpx	53·5	1·52	18·4	8·68	0·13	0·28	8·59	3·17	6·47	0·68	101	51
SR26EcpxOrimMI 30 μm***	cpx	52·8	1·44	17·4	7·77	0·16	4·37	7·98	3·07	5·56	0·86	101	31
SR22MI2cpxD 40 μm***	cpx	57·1	0·59	16·7	6·27	0·25	0·41	7·46	4·66	6·55	—	100	24
SR22MI2cpxC 20 μm***	cpx	57·2	0·67	17·2	5·11	0·13	3·10	7·43	3·72	6·07	—	101	43
SR22MI3cpxE 40 μm***	cpx	54·6	0·75	16·7	6·96	0·16	3·14	7·91	3·87	6·68	—	101	37
SR22MI1apa1 30 μm***	apa	56·4	0·79	17·5	4·91	0·10	1·19	7·74	4·14	7·24	—	100	(56)
SR22MI3apa1 20 μm***	apa	55·1	0·76	17·4	5·71	0·15	1·58	7·99	4·21	7·14	—	100	(312)
SR22MI2apa2 20 μm**(*)	apa	56·0	0·74	16·4	5·59	0·20	1·59	7·82	4·31	7·40	—	100	64
SR22DMI3apa 20 μm***	apa	55·0	0·77	18·0	5·66	0·12	1·15	8·01	3·74	7·56	—	100	59
Hornblende-diorite													
SR27FcpxJMIrim 20 μm***	cpx	66·3	0·50	16·8	3·07	0·15	1·67	3·66	4·13	4·12	0·09	100	62
SR27DMI3cpxH 40 μm	cpx	64·6	0·36	17·5	3·23	0·14	1·81	5·28	3·55	3·32	—	100	69
SR27DMI1cpxH 20 μm***	cpx	66·7	0·22	16·5	1·55	0·20	2·80	3·19	4·21	4·80	0·10	100	79
SR27DMIinapainhbl 40 μm***	apa	61·2	0·41	18·6	5·37	0·10	0·62	6·05	3·88	3·74	—	100	43
SR27MIinapa 30 μm***	apa	60·5	0·50	16·5	8·08	0·17	0·97	6·38	3·98	2·93	—	100	(133)
SR25MIcpx 40 μm***	cpx	64·7	0·28	15·9	5·83	0·27	—	5·12	4·35	3·55	—	100	—
SR25MI3hblBcore 30 μm***	hbl	61·0	—	15·9	5·44	0·05	2·39	6·40	4·77	4·04	—	100	60
Quartz-monzodiorite													
SR8ChblEMI 30 μm***	hbl	73·0	0·40	15·4	1·29	0·04	—	1·47	3·32	5·54	0·01	100	10
SR21DMIapa 50 μm***	apa	75·8	0·12	13·0	0·92	0·005	0·10	0·92	3·72	5·43	—	100	85
StaRita8 MI2qtz 60 μm***	qtz	74·1	0·09	14·0	0·70	0·05	0·07	1·10	0·34	5·42	n.a.	96	24
StaRita8 MI3qtz 60 μm***	qtz	74·3	0·08	14·0	0·73	0·04	0·13	1·07	3·41	5·18	n.a.	99	(30)
StaRita8 MI6qtz 60 μm	qtz	74·3	0·09	14·0	0·70	0·05	0·07	1·08	0·14	5·29	n.a.	96	19
StaRita8 MI7qtz 40 μm*(*)	qtz	74·2	0·08	14·0	0·64	0·06	0·07	1·07	0·12	5·46	n.a.	96	22
StaRita8 MI13qtz 60 μm**(*)	qtz	74·5	0·09	14·0	0·66	0·04	0·07	1·04	0·12	5·10	n.a.	96	20
SR20EMIqtzcore 40 μm***	qtz	75·1	0·10	14·0	0·83	0·05	0·08	0·99	0·04	5·42	—	97	14
SR21EMI2qtzrim 30 μm***	qtz	75·5	0·10	14·0	0·59	0·04	0·08	0·93	3·74	4·97	—	100	(12)
SR21EMI1qtzrim 30 μm***	qtz	75·6	0·10	14·0	0·60	0·05	0·07	0·93	4·30	5·46	—	101	(16)
Rhyodacite													
SR15WMIqtzrim 40 μm***	qtz	75·5	0·07	14·0	0·61	0·05	0·06	0·93	4·12	5·40	n.a.	101	23
SR9KMI2qtzcore 40 μm***	qtz	75·0	0·11	14·0	0·66	0·06	0·07	1·01	0·34	4·82	n.a.	96	25
SR9KMI1qtzcore 60 μm***	qtz	75·4	0·09	14·0	0·68	0·05	0·07	0·95	0·33	5·02	n.a.	97	22

Table 2: Continued

Sample name	V	Cr	Co	Ni	Cu	Rb	Sr	Y	Zr	Nb	Cs	Ba	La	Ce	Ta	Pb	Th
Basaltic andesite																	
SR26MI2cpxArim 20 μm***	38	—	7	—	143	212	645	37	193	6	7	958	n.a.	80	n.a.	13	n.a.
SR26MI3cpxArim 50 μm***	127	—	15	2	140	199	613	32	196	8	7	1050	n.a.	58	n.a.	14	n.a.
SR26MI3cpxAcore 20 μm***	125	—	31	—	252	183	748	23	188	8	7	1076	n.a.	48	n.a.	12	n.a.
SR26MI3cpxBcore 40 μm***	129	16	29	—	245	172	717	22	216	6	6	981	n.a.	54	n.a.	11	n.a.
SR26MI1cpxBcore 40 μm**(*)	84	—	20	6	317	178	698	4	143	6	6	919	n.a.	47	n.a.	—	n.a.
SR26MI1cpxCcore 30 μm***	65	—	12	37	240	174	635	11	126	6	2	915	n.a.	45	n.a.	10	n.a.
SR26DcpxNMI3 30 μm***	n.a.	77	n.a.	24	306	176	712	29	169	7	n.a.	1099	27	54	0·4	13	6
SR26DcpxNMI2 30 μm***	n.a.	(249)	n.a.	98	225	171	672	33	195	8	n.a.	985	23	34	(0·5)	21	5
SR26DcpxNMI1 30 μm***	n.a.	30	n.a.	—	110	166	527	29	200	7	n.a.	894	26	57	(0·8)	11	5
SR26DcpxMMI1 30 μm***	n.a.	28	n.a.	33	131	198	394	18	174	7	n.a.	798	18	34	0·6	10	8
SR26DcpxMMI4 30 μm***	n.a.	—	n.a.	—	112	209	410	19	155	10	n.a.	884	20	42	(1·0)	9	6
SR26AcpxLMIrim 30 μm***	n.a.	(173)	n.a.	15	157	257	411	17	206	10	n.a.	1144	19	40	0·6	15	8
SR26AcpxLMImiddle 30 μm***	n.a.	—	n.a.	35	150	226	596	14	183	7	n.a.	1154	29	52	0·3	14	6
SR26AcpxLMI2core 60 μm***	n.a.	23	n.a.	63	367	222	959	9	218	9	n.a.	1328	36	72	0·3	18	7
SR26AcpxLMI1core 60 μm***	n.a.	7	n.a.	24	482	224	858	43	253	9	n.a.	1316	32	68	0·4	17	6
SR26EcpxOrimMI 30 μm***	n.a.	(390)	n.a.	—	180	198	559	30	219	9	n.a.	1267	32	76	(1·1)	12	6
SR22MI2cpxD 40 μm***	11	—	6	—	134	287	725	51	229	14	11	806	n.a.	76	n.a.	20	n.a.
SR22MI2cpxC 20 μm***	149	(200)	11	(59)	142	196	538	47	187	13	6	1061	n.a.	80	n.a.	17	n.a.
SR22MI3cpxE 40 μm***	168	7	—	61	103	232	414	44	181	7	7	855	n.a.	96	n.a.	18	n.a.
SR22MI1apa1 30 μm***	82	(217)	10	(51)	123	255	—	—	219	10	22	624	—	—	n.a.	16	n.a.
SR22MI3apa1 20 μm***	109	(1100)	18	(330)	74	217	491	—	239	10	6	785	—	—	n.a.	21	n.a.
SR22MI2apa2 20 μm**(*)	47	(2174)	(40)	(413)	190	269	—	45	274	12	7	908	—	—	n.a.	13	n.a.
SR22DMI3apa 20 μm***	n.a.	(297)	n.a.	(111)	140	222	548	—	167	7	n.a.	1200	—	—	(1·1)	9	6
Hornblende-diorite																	
SR27FcpxJMIrim 20 μm***	n.a.	(287)	n.a.	(176)	10	126	579	32	236	9	n.a.	1083	31	71	(1·7)	14	8
SR27DMI3cpxH 40 μm	n.a.	(118)	n.a.	(55)	17	106	492	(4)	173	6	n.a.	826	34	60	0·4	22	8
SR27DMI1cpxH 20 μm***	n.a.	(317)	n.a.	(146)	13	142	524	36	208	7	n.a.	1228	31	63	(1·4)	15	9
SR27DMIinapainhbl 40 μm***	n.a.	(144)	n.a.	(60)	86	104	38	—	199	7	n.a.	953	—	—	0·3	13	6
SR27MIinapa 30 μm***	n.a.	(552)	n.a.	(312)	68	85	76	—	196	9	n.a.	939	—	—	(2·4)	22	—
SR25MIcpx 40 μm***	—	—	2	(41)	7	121	500	20	145	7	4	1116	n.a.	29	n.a.	10	n.a.
SR25MI3hblBcore 30 μm***	110	(143)	21	19	28	131	524	—	130	—	6	862	n.a.	12	n.a.	11	n.a.
Quartz-monzodiorite																	
SR8ChblEMI 30 μm***	n.a.	235	n.a.	(178)	20	131	263	25	72	9	n.a.	669	39	57	0·3	16	15
SR21DMIapa 50 μm***	—	(79)	1	13	19	261	143	—	69	8	13	1031	—	—	—	136	—
StaRita8 MI2qtz 60 μm***	n.a.	n.a.	n.a.	n.a.	35	165	n.a.	6	65	7	5	n.a.	n.a.	n.a.	n.a.	n.a.	n.a.
StaRita8 MI3qtz 60 μm***	n.a.	n.a.	n.a.	n.a.	34	155	n.a.	7	71	6	4	n.a.	n.a.	n.a.	n.a.	n.a.	n.a.
StaRita8 MI6qtz 60 μm	n.a.	n.a.	n.a.	n.a.	5	160	n.a.	6	67	7	4	n.a.	n.a.	n.a.	n.a.	n.a.	n.a.
StaRita8 MI7qtz 40 μm*(*)	n.a.	n.a.	n.a.	n.a.	17	158	n.a.	5	64	6	5	n.a.	n.a.	n.a.	n.a.	n.a.	n.a.
StaRita8 MI13qtz 60 μm**(*)	n.a.	n.a.	n.a.	n.a.	17	146	n.a.	6	69	7	4	n.a.	n.a.	n.a.	n.a.	n.a.	n.a.
SR20EMIqtzcore 40 μm***	5	(30)	(0·4)	(10)	13	185	252	6	70	8	3	1368	n.a.	44	n.a.	16	n.a.
SR21EMI2qtzrim 30 μm***	4	(40)	(0·4)	(10)	34	148	249	7	74	6	4	1265	n.a.	42	n.a.	14	n.a.
SR21EMI1qtzrim 30 μm***	5	(44)	(0·5)	(15)	45	171	225	6	65	7	5	874	n.a.	31	n.a.	18	n.a.
Rhyodacite																	
SR15WMIqtzrim 40 μm***	3	(43)	(0·5)	(17)	(2)	143	228	4	51	6	6	1312	n.a.	22	n.a.	27	n.a.
SR9KMI2qtzcore 40 μm***	4	(33)	(0·4)	(8)	8	155	383	7	66	8	4	1335	n.a.	47	n.a.	16	n.a.
SR9KMI1qtzcore 60 μm***	4	(11)	0·4	(4)	4	160	249	6	61	8	5	982	n.a.	44	n.a.	14	n.a.

All values in ppm, except for elements listed as wt % oxides. The anhydrous totals of some qtz-hosted inclusions are low because of loss of Na. Numbers in parentheses denote detection limits. n.a., not analyzed; —, elements for which the host correction returned negative values. The number of stars at the end of the sample names is a measure of the quality of the ablation process (three stars corresponding to a perfect ablation), and the size refers to the crater diameter (which typically was about 1·2–1·5 times the inclusion diameter).

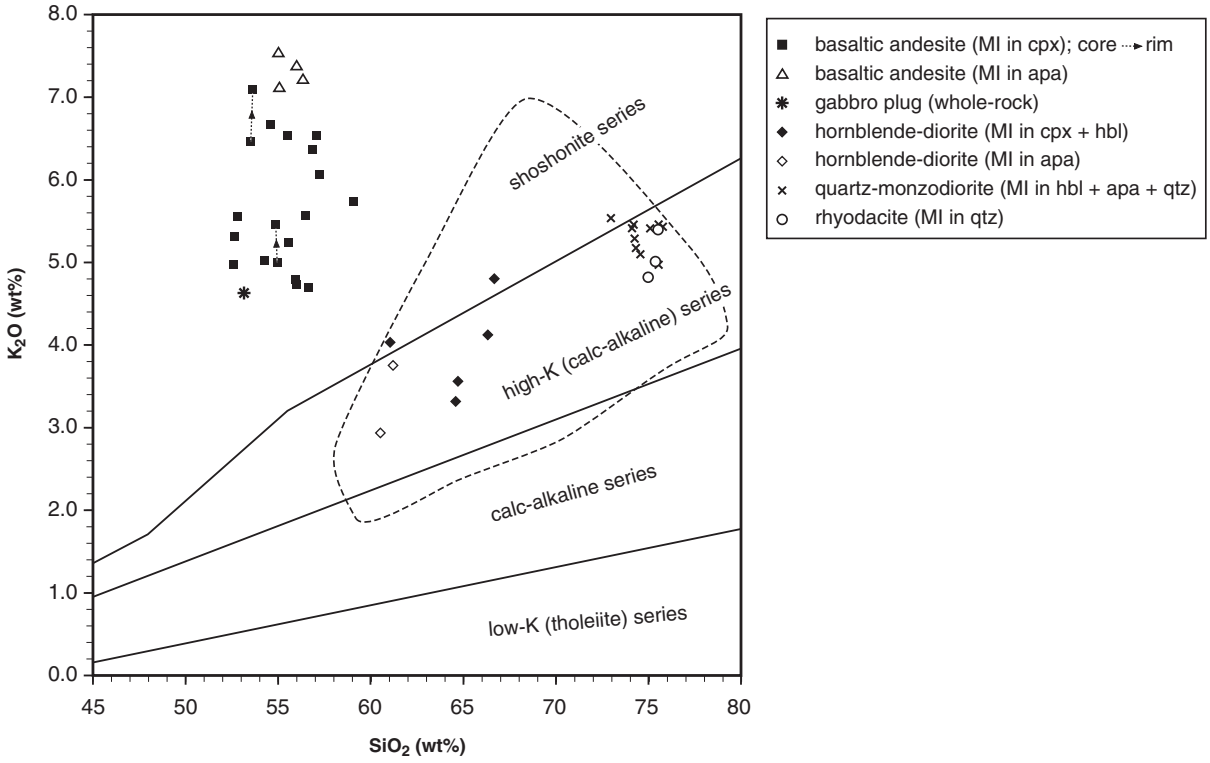

Fig. 4. Composition of whole-rocks and silicate melt inclusions from various rock types associated with the Santa Rita magmatic system. The array of whole-rock analyses published in Jones *et al.* (1967) is indicated by the dashed line, with the exception of the gabbro plug, which is shown separately. Remaining symbols represent melt inclusion (MI) compositions as reconstructed from LA-ICP-MS analyses. Core-to-rim trends of melt inclusions within single phenocrysts are indicated by dotted arrows. Boundary lines between series are from Rickwood (1989). (For abbreviations see Table 1.)

& Hanghøj, 2004). The fact that the composition of apatite-hosted melt inclusions is very similar to that of augite-hosted melt inclusions (Table 2) demonstrates that these compositions are real and not a result of boundary-layer effects, post-entrapment modifications or improper LA-ICP-MS signal deconvolution.

The presence of rare sulfide droplets next to silicate melt inclusions in augite phenocrysts suggests that the magma was, at least temporarily, sulfide saturated. The two sulfide inclusions analyzed from this rock are characterized by very high Cu contents (45 wt % Cu; Table 3).

Hornblende-diorite porphyry

Hand specimens of hornblende-diorite porphyry dikes can be grouped into two textural types. One type (samples SR23, SR25, SR27) contains black, lustrous hornblende laths of up to 5 mm length (10–15 vol. %) as well as plagioclase crystals of 1–2 mm size (20–30 vol. %; $An_{40–50}$) set in a greenish gray, aphanitic groundmass (Fig. 5). Less abundant are phenocrysts of magnetite (2–3 vol. %), apatite (<1 vol. %) and either augite (3–6 vol. %) or biotite (3–6 vol. %). The other type (samples SR24, SR28; not discussed further) contains less phenocrysts (10–15 vol. % in total) and larger plagioclase crystals (up to 5 mm), but otherwise has identical characteristics to the crystal-rich variety. Magmatic sulfides are very abundant in these rocks and can be observed in nearly all augite or hornblende phenocrysts. The high abundance of magmatic sulfides in the hornblende-diorite porphyry is in strong contrast to the basaltic andesite, where about 50–100 phenocrysts had to be examined to find a single sulfide inclusion. Most of the melt inclusions in clinopyroxene, hornblende and apatite contain 61–67 wt % SiO_2, 0·8–2·8 wt % MgO, 3·1–5·8 wt % FeO and 2·9–4·8 wt % K_2O. The average Cu content of these melts is significantly lower than those analyzed from the basaltic andesite (38 ppm vs 191 ppm), which can be explained by the higher abundance of magmatic sulfides in the hornblende-diorite (see below).

Two samples from the crystal-rich variety of hornblende-diorite porphyry (SR25, SR27) contain abundant, partly dissected enclaves of up to 30 mm size that can be distinguished from the matrix by their smaller grain size and higher content of mafic minerals (Fig. 5a). This observation, together with the presence of irregular, mafic cores in some of the

Table 3: LA-ICP-MS analyses of sulfide inclusions

Sample name	Type*	S† (wt %)	Fe (wt %)	Co (wt %)	Ni (wt %)	Cu (wt %)	Ba (ppm)	Pb (ppm)	Au (ppm)	Zn (ppm)	As (ppm)	Se (ppm)	Mo (ppm)	Ag (ppm)
Basaltic andesite														
SR26DcpxMsulf2 14 μm		35·0	19·2	n.a.	0·56	45·8	111	829	n.a.	n.a.	n.a.	n.a.	n.a.	n.a.
SR26DcpxMsulf1 14 μm		35·2	19·6	n.a.	0·79	45·2	154	1073	n.a.	n.a.	n.a.	n.a.	n.a.	n.a.
Hornblende diorite														
SR23XhblDsulfiderim 20 μm	B	36·5	58·1	0·13	0·11	5·4	(5)	2	(1·0)	120	(10)	45	(7)	3
SR23XhblDsulfidecore 20 μm	B	36·5	57·5	0·18	0·06	6·0	(13)	(16)	(4·8)	(86)	(41)	(193)	(19)	(9)
SR23XhblCsulfide1 30 μm	B	36·5	57·9	0·14	0·17	5·6	(4)	1	(1·1)	188	(12)	60	(5)	4
SR23XhblCsulfide2 30 μm	B	36·6	58·1	0·17	0·18	5·3	(5)	6	(1·8)	113	(9)	94	(10)	5
SR23XhblCsulfide3 20 μm	B	36·6	57·7	0·14	0·20	5·8	(19)	4	(6·5)	255	(43)	(168)	(27)	(6)
SR23XhblCsulfide4 50 μm	A	36·6	60·4	0·16	0·13	3·0	1896	703	(3·8)	498	112	83	106	204
SR23XhblCsulfide5 30 μm	A	36·7	60·0	0·15	0·16	3·4	305	993	(1·3)	444	88	79	36	58
SR23XhblCsulfide6 30 μm	B	36·6	58·5	0·17	0·17	4·8	(4)	7	(2·0)	79	(16)	66	(14)	5
SR23XhblDsulfide1 50 μm	A	37·2	60·1	0·64	0·20	2·7	2182	1235	3·7	375	460	111	61	715
SR23XhblDsulfide2 50 μm	B	36·5	58·5	0·12	0·08	5·0	(4)	(2)	(0·6)	95	(7)	52	(4)	(1)
SR23XhblEsulfide1 50 μm	A	36·8	61·6	0·23	0·16	1·6	2258	611	0·8	533	59	58	44	25
SR23XhblEsulfide2 50 μm	B	36·6	58·9	0·16	0·13	4·5	(12)	3	(2·4)	692	(22)	46	(7)	(5)
SR25sulfidehblA 30 μm	B	36·6	62·3	0·12	0·07	1·1	(7)	2	n.a.	n.a.	n.a.	n.a.	n.a.	n.a.
SR25sulfide2hblBcore 30 μm	B	36·8	59·8	0·29	0·16	3·4	(55)	(97)	n.a.	n.a.	n.a.	n.a.	n.a.	n.a.
SR25sulfide1hblBcore 20 μm	B	36·7	61·9	0·13	0·11	1·5	(8)	(11)	n.a.	n.a.	n.a.	n.a.	n.a.	n.a.
SR27AcpxAsulfide 30 μm	B	36·6	61·6	0·08	0·11	1·8	(18)	54	n.a.	n.a.	n.a.	n.a.	n.a.	n.a.
SR27sulfidehblcore 20 μm	B	36·7	61·5	0·19	0·10	1·8	(7)	3	n.a.	n.a.	n.a.	n.a.	n.a.	n.a.
SR27sulfidehblrim 20 μm	B	36·7	61·8	0·12	0·11	1·5	(14)	0	n.a.	n.a.	n.a.	n.a.	n.a.	n.a.
SR27FcpxJsulfiderim1 30 μm	B	36·5	61·8	n.a.	0·07	1·7	(14)	13	n.a.	n.a.	n.a.	n.a.	n.a.	n.a.
SR27FcpxJsulfiderim2 14 μm	B	36·4	62·0	n.a.	(0·14)	1·6	(40)	(23)	n.a.	n.a.	n.a.	n.a.	n.a.	n.a.
SR27Bsulfideincpx 14 μm	B	36·4	62·2	n.a.	(0·03)	1·4	(26)	(14)	n.a.	n.a.	n.a.	n.a.	n.a.	n.a.
Rhyodacite														
SR15hblCsulf 14 μm		36·5	63·4	n.a.	(0·10)	0·1	(53)	(26)	n.a.	n.a.	n.a.	n.a.	n.a.	n.a.
SR15hblBsulf 14 μm		36·4	60·9	n.a.	(0·28)	2·8	191	(129)	n.a.	n.a.	n.a.	n.a.	n.a.	n.a.
SR15hblAsulf2 14 μm		36·4	61·1	n.a.	(0·11)	2·5	(66)	(40)	n.a.	n.a.	n.a.	n.a.	n.a.	n.a.
SR15hblAsulf3 20 μm		35·4	40·5	n.a.	(0·60)	24·1	(357)	(286)	n.a.	n.a.	n.a.	n.a.	n.a.	n.a.

Numbers in parentheses represent detection limits.
*Sulfides from the hornblende diorite porphyry are classified into two types based on their content of Fe, Cu and trace elements.
†Calculated based on the assumption that Fe, Co, Ni and Cu are present as FeS, CoS, NiS and CuS, respectively.

pyroxene phenocrysts (Fig. 5b), suggests that the hornblende-diorite porphyry formed by magma mixing. Another sample from this rock type (SR23) contains dark, angular xenoliths of up to 30 cm size that consist almost exclusively of coarsely crystallized hornblende. Minor other phases present in these hornblende xenoliths comprise apatite, magnetite, resorbed relicts of biotite, and numerous sulfide inclusions. LA-ICP-MS analyses of sulfide inclusions arranged along a single growth zone within individual hornblende crystals reveal two chemically distinct sulfide phases. Both have roughly the composition of pyrrhotite, with one (Type B) containing 4·5–6·0 wt % Cu, and the other (Type A) containing 1·5–3·4 wt % Cu but up to 100 times higher amounts of Ag, Mo, Pb, As and Ba, as well as traces of gold (Table 3).

Quartz-monzodiorite porphyry

Samples of quartz-monzodiorite porphyry [corresponding to the 'granodiorite porphyry dikes' described by Jones *et al.* (1967)] are greenish gray in color and contain phenocrysts of plagioclase (15–25 vol. %; $An_{20–45}$), hornblende (5–15 vol. %), biotite (3–7 vol. %), quartz

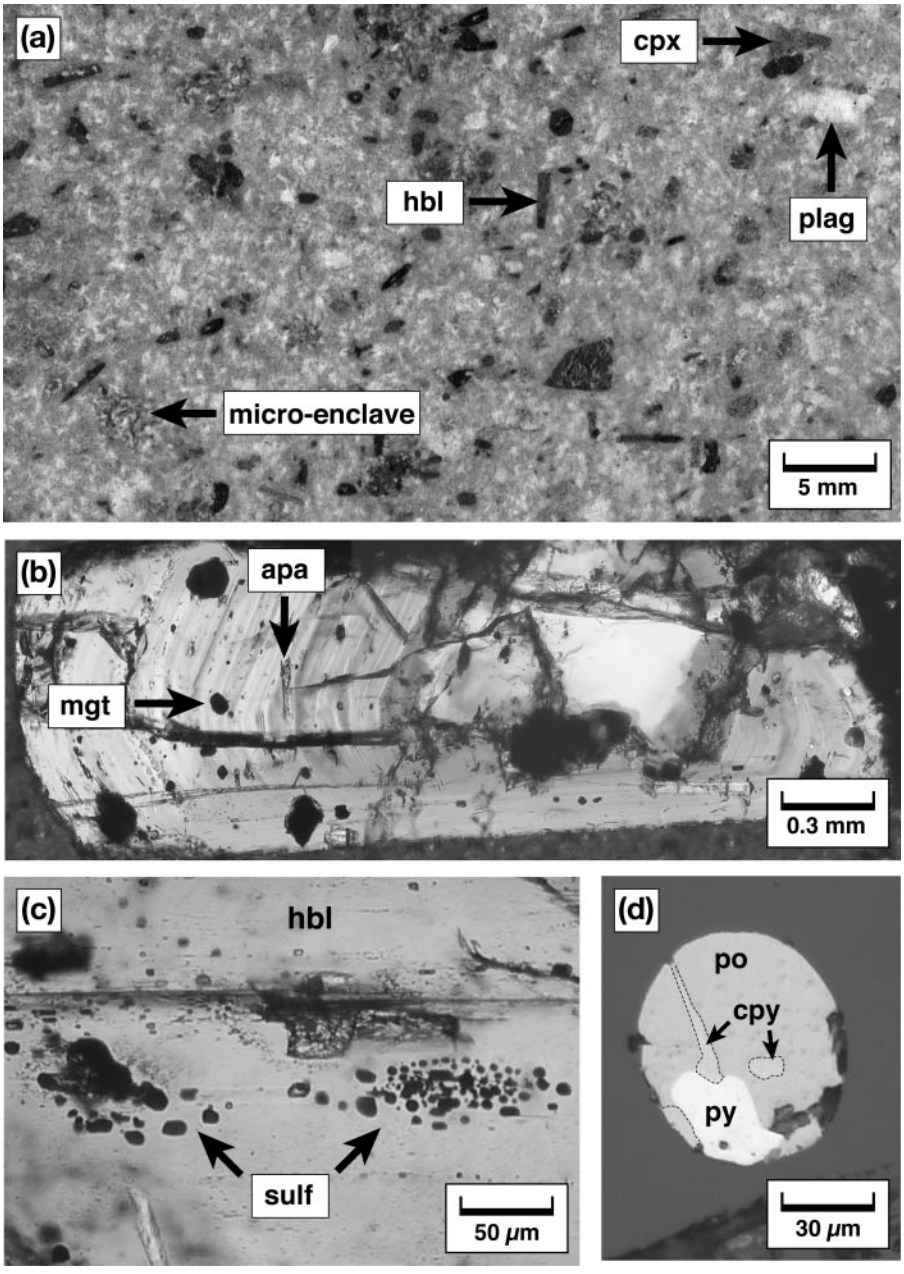

Fig. 5. Petrography of hornblende-diorite porphyry. (a) Photograph of a polished surface of hand specimen SR27. (b) Thick section through a zoned augite phenocryst from sample SR27. The augite phenocryst contains an irregular, mafic core that is recognizable by its lighter color (transmitted light). (c) Primary sulfide inclusions within hornblende (sample SR27; transmitted light). (d) Exposed part of a sulfide inclusion in hornblende (sample SR23; reflected light; po, pyrrhotite; py, pyrite; cpy, chalcopyrite).

(2–4 vol. %), and ≤1vol. % of magnetite, titanite and apatite set in an aphanitic groundmass (Fig. 6; Table 1). Additionally, the rock originally contained 1–2 vol. % anhydrite (now present as lath-shaped cavities filled with either microcrystalline quartz or calcite; Audétat *et al.*, 2004), and 2–4 vol. % of mafic minerals that are replaced by chlorite and magnetite. Primary mineral inclusions identified in phenocryst phases comprise magmatic anhydrite, sulfides, zircon, allanite, clinopyroxene, olivine, ilmenite and calcite (Table 1). Microprobe and LA-ICP-MS analyses of 28 amphibole phenocrysts and six amphibole inclusions in quartz and apatite reveal the existence of two chemically distinct hornblende populations that show no overlap in terms of core–rim zonations (Fig. 7). The less mafic hornblende population contains 30–45 ppm Ni and <50 ppm Cr,

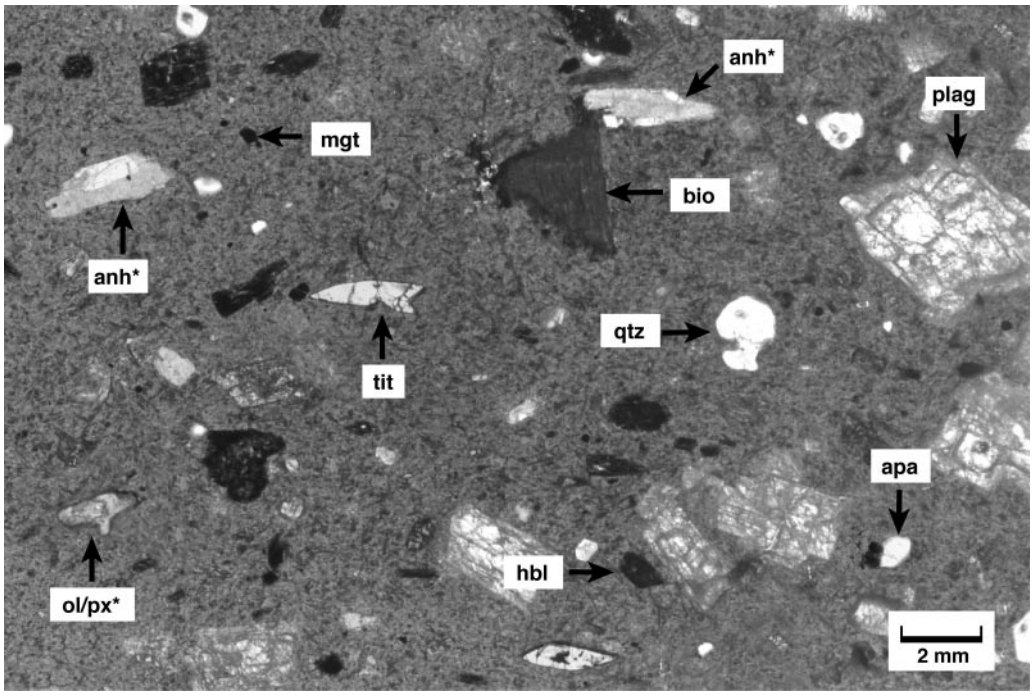

Fig. 6. Transmitted-light image of a thick section of quartz-monzodiorite porphyry sample SR20, showing all major phenocryst phases present in this rock (anh*, decomposed anhydrite; ol/px*, decomposed olivine or pyroxene; see Table 1 for other abbreviations).

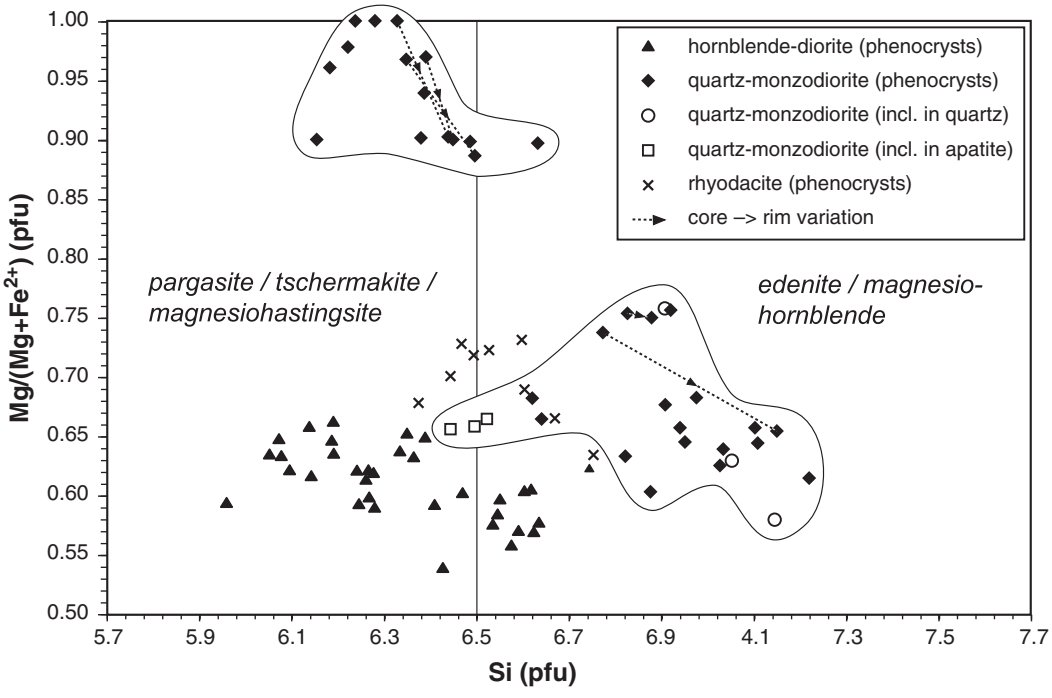

Fig. 7. Composition of hornblende crystals (*sensu lato*) analyzed from Santa Rita, recalculated using the method of Holland & Blundy (1994). The data for the quartz-monzodiorite can be grouped into two distinct populations (circled fields) that do not overlap in terms of core–rim variations. The nomenclature is after Leake *et al.* (1997).

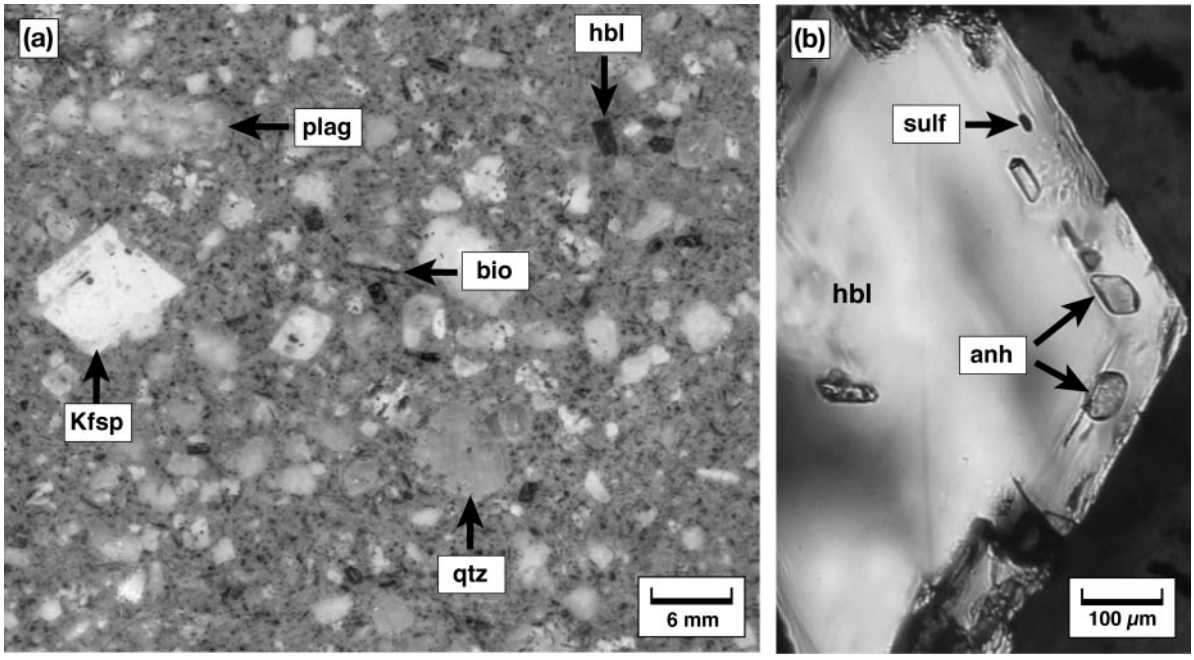

Fig. 8. Petrography of the rhyodacite porphyry: (a) photograph of a polished surface of hand specimen SR15; (b) hornblende phenocryst containing inclusions of anhydrite (anh) and sulfide (sulf) (transmitted light).

and hosts inclusions of anhydrite. Hornblende inclusions in quartz and apatite phenocrysts are always of this type. The more mafic hornblende population contains 150–780 ppm Ni and 500–11 000 ppm Cr, hosts inclusions of olivine (Fo_{84}) and Mg-rich clinopyroxene, and typically is intergrown with altered mafic phenocrysts. The latter therefore probably represent altered olivine and clinopyroxene phenocrysts.

The lack of any compositional overlap between the two hornblende populations on the scale of single phenocrysts strongly suggests that the quartz-monzodiorite porphyry preserves a disequilibrium mineral assemblage after an event of magma mixing. This interpretation is supported by the fact that the phenocryst assemblage in the quartz-monzodiorite porphyry is too varied to represent an equilibrium assemblage (e.g. quartz and olivine occur together in the same rock), and that the melt inclusions in quartz phenocrysts are more silicic (73–75 wt % SiO_2; Table 2) than the rock groundmass. The latter contains only 66–68 wt % SiO_2 (calculated from the composition of the bulk rock minus the contained phenocrysts). Hence, the melt trapped in quartz-hosted inclusions cannot be a fractional crystallization product of the bulk magma, but needs to originate from a more evolved magma. The composition of the quartz-hosted melt inclusions in the quartz-monzodiorite porphyry is identical to that of quartz-hosted melt inclusions in the rhyodacite (Table 2), suggesting that this evolved magma may have had a composition similar to that of the rhyodacite.

Magmatic sulfide inclusions seem to be very rare in the quartz-monzodiorite magma. The only three intact sulfide inclusions found are hosted by the more primitive, Mg-rich hornblende population.

Rhyodacite porphyry

Hand specimens of rhyodacite porphyry (SR15) are light green to light gray in color and are characterized by the presence of phenocrysts of plagioclase (20–40 vol. %; up to 6 mm in diameter; An_{22}), potassic feldspar (1–3 vol. %; up to 12 mm), quartz (2–8 vol. %, maximum 7 mm), hornblende (3–10 vol. %), biotite (1–5 vol. %), and <1 vol. % each of magnetite, apatite, titanite and ilmenite (Fig. 8a). In addition, petrographic relationships similar to those described by Audétat *et al.* (2004) suggest that the magma originally contained 1–3 vol. % anhydrite phenocrysts, which are still recognizable as lath-shaped cavities filled with calcite. Fresh magmatic anhydrite is preserved as inclusions within other phenocrysts, where it occurs together with inclusions of magmatic sulfides, magnetite, titanite, zircon and allanite (Fig. 8b; Table 1).

Both Cu-rich and Cu-poor sulfide inclusions have been identified in the hornblende phenocrysts (Table 3). The fact that inclusions of magmatic anhydrite and sulfides commonly occur along the same growth zone demonstrates that the magma contained both reduced and oxidized forms of condensed sulfur.

THERMOBAROMETRY

The following methods were used to estimate pre-emplacement crystallization conditions of the magmas: (1) olivine–magnetite–clinopyroxene equilibria (using QUILF program; Andersen *et al.*, 1993); (2) apatite saturation thermometry (based on the P_2O_5 content of melt inclusions; Harrison & Watson, 1984); (3) zircon saturation thermometry (based on the Zr content of melt inclusions; Watson & Harrison, 1983); (4) hornblende–plagioclase thermometry (Holland & Blundy, 1994); (5) Al-in-hornblende barometry (Anderson & Smith, 1995); (6) clinopyroxene–hornblende thermometry (Perchuk *et al.*, 1985; as discussed by Anderson, 1996); (7) magnetite–ilmenite equilibria (QUILF program). The results (summarized in Table 4) are discussed in detail below.

Table 4: Summary of thermobarometry results

Magma type, method	*n**	*T* (°C)	log f_{O_2}	*P* (kbar)
Basaltic andesite				
ol–mgt–px (QUILF)	7/4/6	1020–1070	NNO + 0·7 to NNO + 1·5	
apatite saturation	9	910–1020		
Hornblende-diorite				
apatite saturation	2	850–870		
cpx–hbl	25/12	880		
plag–hbl	8/12	750–800		
Quartz-monzodiorite				
(felsic endmember only)				
apatite saturation	1	730		
zircon saturation	8	720–750		
plag–hbl	3/4	700		
Al-in-hbl	4			1·6–3·9
Rhyodacite				
zircon saturation	3	730–750		
mgt–ilm (QUILF)	11/11	730 ± 60	NNO + 1·3 to NNO + 1·9	

*Number of grains analyzed (minerals separated by slashes). Abbreviations are the same as in Table 1.

Basaltic andesite

Equilibrium between olivine, augite and magnetite allows two of the four parameters f_{O_2}, a_{SiO_2}, P and T to be calculated if the other two parameters are known (Lindsley & Frost, 1992). However, even if none of these parameters is known, reasonable T and f_{O_2} values can be obtained if f_{O_2} is designated as a variable, and pressure is fixed. Olivine, augite and magnetite in textural equilibrium were found in sample SR26, in which inclusions of olivine and magnetite occur next to each other along growth zones in phenocrystic augite. The olivine and magnetite inclusions are compositionally homogeneous, showing no signs of exsolution or reaction rims. Augite compositions were determined both next to the analyzed inclusions and on the phenocryst rim to account for potential re-equilibration effects. Representative microprobe analyses and corresponding results are given in Table 5.

Temperatures and oxygen fugacities calculated at 1 kbar and with the augite composition next to the analyzed inclusions range from 1020°C to 1070°C and $\log f_{O_2}$ = NNO + 0·7 to $\log f_{O_2}$ = NNO + 1·5, respectively. The effect of changing pressure is negligible, producing an increase of 2–3°C/kbar and having no effect on the calculated oxygen fugacity. The compositional variation between augite rims and augite hosts next to the analyzed inclusions affects the calculated temperatures by less than 30°C. It should be noted that the reconstructed oxygen fugacity does not stand in contradiction to the (rare) presence of sulfide inclusions in this rock, as sulfide saturation can be achieved also at relatively oxidized conditions (e.g. Scaillet & Evans, 1999; DeHoog *et al.*, 2004).

An independent temperature estimate was obtained from the P_2O_5 content of melt inclusions using the apatite saturation geothermometer of Harrison & Watson (1984). Calculated temperatures should correspond to true entrapment temperatures because the ubiquitous presence of apatite inclusions in the augite phenocrysts demonstrates that the melt was saturated in apatite at that stage. Apatite saturation temperatures obtained from melt inclusions in augite from sample SR26 range from 910°C to 1020°C, with values decreasing from core to rim. The higher end of this range agrees well with the temperatures obtained from olivine–clinopyroxene–magnetite equilibria.

Experiments on compositionally similar (but less K-rich) melts have shown that the crystallization sequence (olivine + augite + magnetite) → (olivine + augite + magnetite + plagioclase), which is indicated by the mineralogy of samples SR26 and SR22, occurs in the range 1000–1050°C and 1·3–2·3 kbar (Moore & Carmichael, 1998), consistent with the temperature estimates presented above.

Hornblende-diorite porphyry

The pre-emplacement crystallization temperature of the hornblende-diorite magma is estimated at 850–880°C on the basis of apatite saturation thermometry and clinopyroxene–hornblende thermometry (Table 4). Plagioclase–hornblende thermometry yields significantly lower temperatures of 750–800°C, which might be a consequence of the fact that the measurable plagioclase and hornblende grains were not in textural equilibrium.

Table 5: Selected microprobe data and corresponding results calculated with QUILF

Sample:	rhyodacite (SR15)		basaltic andesite (SR26; augite phenocryst J)				basaltic andesite (SR26; augite phenocryst L)				basaltic andesite (SR26; average of all analyses)			
Mineral:	magnetite	ilmenite	magnetite	olivine	augite syng.*	augite rim	magnetite	olivine	augite syng.*	augite rim	magnetite	olivine	augite syng.*	augite rim
Analyses:	11	11	1	1	2	2	3	6	3	2	6	16	15	8
Grains:	6	7	1	1	1	1	2	1	1	1	4	7	6	3
SiO_2	0·05 ± 0·08	0·003 ± 0·01	0·12	36·85	49·97 ± 0·02	49·54 ± 0·74	0·11 ± 0·04	37·45 ± 0·14	50·27 ± 0·37	49·06 ± 0·23	0·09 ± 0·06	37·48 ± 0·38	49·81 ± 0·58	49·55 ± 0·50
Na_2O	n.a.	n.a.	n.a.	<0·01	0·38 ± 0·01	0·51 ± 0·07	n.a.	0·01 ± 0·01	0·46 ± 0·07	0·48 ± 0·03	n.a.	0·01 ± 0·01	0·42 ± 0·04	0·48 ± 0·03
TiO_2	4·97 ± 0·56	37·42 ± 0·70	10·08	0·05	0·77 ± 0·14	0·98 ± 0·20	10·68 ± 0·16	0·03 ± 0·01	0·79 ± 0·08	1·19 ± 0·06	10·41 ± 0·30	0·02 ± 0·02	0·88 ± 0·10	1·03 ± 0·14
MnO	1·12 ± 0·11	2·12 ± 0·44	0·35	0·56	0·28 ± 0·02	0·30 ± 0·04	0·38 ± 0·01	0·51 ± 0·01	0·25 ± 0·04	0·28 ± 0·03	0·37 ± 0·02	0·53 ± 0·04	0·24 ± 0·03	0·28 ± 0·02
Al_2O_3	1·23 ± 0·28	0·18 ± 0·03	7·91	0·01	3·49 ± 0·14	4·13 ± 0·49	8·34 ± 0·81	0·03 ± 0·01	4·06 ± 0·59	4·65 ± 0·37	8·29 ± 0·65	0·03 ± 0·01	4·03 ± 0·36	4·14 ± 0·50
MgO	0·44 ± 0·28	1·16 ± 0·18	4·54	33·63	14·29 ± 0·18	13·75 ± 0·23	4·55 ± 0·27	35·66 ± 0·22	14·22 ± 0·14	13·14 ± 0·22	4·68 ± 0·25	34·29 ± 0·93	13·95 ± 0·26	13·61 ± 0·42
FeO	86·50 ± 0·70	57·21 ± 0·47	71·43	29·30	8·83 ± 0·10	9·99 ± 0·30	71·15 ± 0·92	26·79 ± 0·25	9·24 ± 0·72	9·98 ± 0·16	71·04 ± 0·68	28·21 ± 1·08	9·03 ± 0·23	9·90 ± 0·15
CaO	n.a.	n.a.	n.a.	0·45	20·82 ± 0·52	20·05 ± 0·62	n.a.	0·36 ± 0·02	20·50 ± 1·09	20·73 ± 0·01	n.a.	0·38 ± 0·05	20·92 ± 0·32	20·51 ± 0·40
Cr_2O_3	n.a.	n.a.	0·11	n.a.	n.a.	n.a.	0·10 ± 0·03	n.a.	n.a.	n.a.	0·11 ± 0·03	n.a.	n.a.	n.a.
Total	94·32 ± 0·33	98·09 ± 0·34	94·54	100·85	98·82 ± 0·28	99·23 ± 0·08	95·31 ± 0·09	100·83 ± 0·15	99·81 ± 0·15	99·50 ± 0·16	94·99 ± 0·39	100·95 ± 0·21	99·28 ± 0·36	99·49 ± 0·25
P set	1 kbar				1 kbar				1 kbar				1 kbar	
T (°C)	762 ± 61†				1056 ± 9				1016 ± 104				1062 ± 110	
a_{SiO_2}					0·75				—				—	
ΔNNO	2·3 ± 0·8†				0·7 ± 0·1				1·5 ± 1·5				1·3 ± 1·4	
P set	5 kbar				5 kbar				5 kbar				5 kbar	
T (°C)	762 ± 61†				1069 ± 13				1022 ± 71				1072 ± 75	
a_{SiO_2}					0·67				0·95				0·9	
ΔNNO	2·1 ± 0·8†				0·8 ± 0·2				1·5 ± 1·0				1·3 ± 1·0	

*Augite from the same growth zone as the analyzed magnetite and olivine inclusions.
†In the rhyodacite, calculated temperatures and oxygen fugacities are likely to be too high by 20–50°C and 0·2–0·8 log units f_{O_2}, respectively (see text for further explanation).

Phase equilibrium studies of the compositionally similar Fish Canyon Tuff demonstrate that the assemblage clinopyroxene + hornblende + plagioclase (without biotite) is stable at 800–890°C and ≤1·8 kbar at a water activity of $a_{H_2O} = 1·0$, and at 850–900°C and ≤2·3 kbar at $a_{H_2O} = 0·5$ (Johnson & Rutherford, 1989). The hornblende-diorite magma, therefore, probably crystallized at 850–880°C and ≤2·3 kbar before dike emplacement.

Quartz-monzodiorite porphyry

Because of the relatively poor preservation of this rock type we could use only quartz-hosted mineral and melt inclusions for thermobarometry. As a consequence, only the felsic component involved in the formation of this rock is considered in this section. Zircon saturation temperatures of 718–750°C obtained from eight melt inclusions agree well with the single apatite saturation temperature of 734°C. Ubiquitous zircon and apatite inclusions in the quartz phenocrysts suggest that the magma was saturated in these two minerals. A third temperature estimate provided by plagioclase–hornblende thermometry (650–750°C) is again not very reliable because the analyzed four hornblende inclusions and three plagioclase inclusions were not in textural equilibrium. The felsic component of the quartz-monzodiorite porphyry probably meets the requirements for the application of the Al-in-hornblende barometer of Anderson & Smith (1995). This barometer, calibrated on the low-variance mineral assemblage quartz, K-feldspar, $An_{25–35}$ plagioclase, biotite, hornblende [Fe/(Fe + Mg) <0·65], titanite and Fe–Ti oxide in the presence of melt and a free vapor phase, yields a formation pressure of 1·6–3·9 kbar.

For the mafic component of the quartz-monzodiorite porphyry a relatively high crystallization temperature (equal to or higher than that of the basaltic andesite) is indicated by the mafic nature of the corresponding hornblende population and the presence of olivine inclusions of Fo_{84} in these phenocrysts.

Rhyodacite porphyry

Microprobe analyses of 11 ilmenite grains and 11 titanomagnetite grains were used to calculate T and f_{O_2} with the QUILF package (Andersen *et al.*, 1993). The analyzed ilmenite and magnetite phenocrysts are free of exsolution features, but are partially altered to hematite and rutile along their rims. The unaltered parts fulfill the Mg/Mn partitioning test of Bacon & Hirschmann (1988) for equilibrium. Two compositionally distinct magnetite types were found to be present in the rhyodacite, of which only one is genetically related to the ilmenite (the other not being used for calculation). Magnetite–ilmenite thermometry suggests a temperature of 762 ± 61°C, in agreement with zircon saturation temperatures of 727–748°C obtained from three melt inclusions in quartz phenocrysts. Corresponding oxygen fugacities range from $\log f_{O_2} = NNO + 2·1$ to $NNO + 2·3$. It should be noted, however, that current solution models for two-oxide equilibria [i.e. QUILF and the formulation of Ghiorso & Sack (1991)] tend to return erroneous temperatures and too high f_{O_2} values at oxygen fugacities greater than NNO + 1 (Evans & Scaillet, 1997; Scaillet & Evans, 1999; Lattard *et al.*, 2005). For the compositionally similar oxide pairs from Mt. Pinatubo QUILF returns more accurate results than the formulation of Ghiorso & Sack (1991), but still overestimates temperature by 20–50°C and f_{O_2} by 0·2–0·8 log-units (Lattard *et al.*, 2005). We therefore regard a temperature of 730 ± 60°C and an oxygen fugacity of NNO + 1·3 to NNO + 1·9 as more realistic results for the rhyodacite porphyry. These f_{O_2} values are about 1·1 log-units above the boundary between SO_4^{2-} and S^{2-} dominance of dissolved sulfur species in silicate melts (Wallace & Carmichael, 1994; Fig. 9).

In summary, the rhyodacitic magma appears to have equilibrated at 730–760°C and an oxygen fugacity of $\log f_{O_2} = NNO + 1·3$ to $NNO + 1·9$ before dike emplacement. These conditions are very similar to those reported for the anhydrite-bearing dacite at Mt. Pinatubo (Scaillet & Evans, 1999), but considerably cooler than those of the less silicic, anhydrite-bearing magmas described from El Chichón (Luhr, 1990), Lascar Volcano (Matthews *et al.*, 1999*b*), and Eagle Mountain (Parat *et al.*, 2002; Fig. 9).

RECONSTRUCTED MAGMA EVOLUTION

The relative importance of magma mixing vs fractional crystallization in the Santa Rita magmatic system is now investigated. Magma evolution in the basaltic andesite is best monitored by K_2O because none of the phenocryst phases present in this rock incorporated significant amounts of this component (cpx 0·002 wt %; ol <0·003 wt %; ap <0·002 wt %; plag 0·57 wt %; all measurements by LA-ICP-MS). Potassium, therefore, behaved very incompatibly. Melt inclusion compositions reveal a clear trend of increasing K_2O content from plagioclase-free sample SR26 to plagioclase-bearing sample SR22, and from core to rim within individual phenocrysts (Table 2, Fig. 4). This observation suggests that sample SR22 evolved through fractional crystallization from sample SR26, which is in accord with the crystallization sequence and phase equilibrium considerations discussed above.

Melt inclusions from the hornblende-diorite porphyry are characterized by distinctly lower K_2O contents

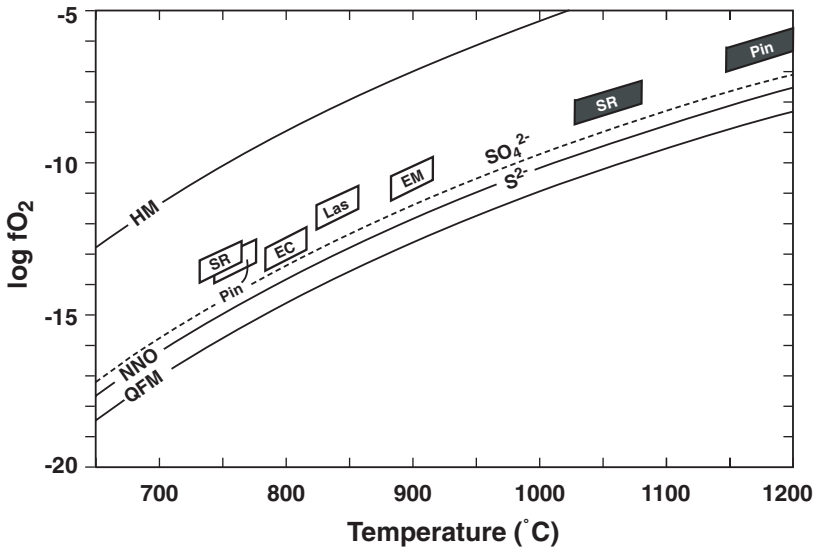

Fig. 9. Estimated T–f_{O_2} conditions of the most felsic (white boxes) and most mafic (black boxes) magmas found at Santa Rita (SR), compared with estimates for other anhydrite-bearing magmas and corresponding mafic counterparts. Pin, Mt. Pinatubo (Scaillet & Evans, 1999; DeHoog *et al.*, 2004); EC, El Chichón (Luhr, 1990); Las, Lascar Volcano (Matthews *et al.*, 1999*b*); EM, Eagle Mountain (Parat *et al.*, 2002). Reaction curves of f_{O_2} buffer assemblages (continuous lines; HM, hematite-magnetite; NNO, Ni–NiO; QFM, quartz–fayalite–magnetite) and the boundary between SO_4^{2-} and S^{2+} predominance in silicate magmas (dashed line) are from Chou (1987) and Wallace & Carmichael (1994), respectively.

Table 6: Core–rim zonations in augite phenocrysts

Magma type	Crystal part	MgO (wt %)	Cr (ppm)	Ni (ppm)
basaltic andesite	core	14·6	660	90
	rim	12·6	60	50
hornblende-diorite	core	16·8	3700	200
	rim	13·1	<47	<12

(2·9–4·8 wt % K_2O) and higher SiO_2 contents (55–65 wt % SiO_2) than those present in the basaltic andesite. This precludes them from being a fractional crystallization product of the basaltic andesite unless large amounts of biotite (or another K-rich mineral) had crystallized in the mean time. Biotite is absent from the samples from which the melt inclusions were analyzed. Hence, it is unlikely that biotite crystallization was responsible for the lower K content in the hornblende-diorite porphyry. Rather, the presence of enclaves and corroded augite cores in this rock points to an origin by magma mixing. This interpretation is supported by the fact that augite cores in the hornblende-diorite porphyry are more mafic than the augite rims in the basaltic andesite (Table 6), which would not be the case if the hornblende-diorite was a fractional crystallization product of the basaltic andesite. The K_2O vs SiO_2 relationship displayed in Fig. 4 suggests that the felsic end-member involved in the formation of the hornblende-diorite magma may have had a composition similar to the rhyodacite, and that the mafic end-member was at least as primitive as (but less potassium-rich than) the basaltic andesite.

A similar picture emerges for the quartz-monzodiorite porphyry. It has been shown above that two compositionally distinct hornblende types occur in this rock. The mafic type is characterized by high levels of MgO (up to 17 wt %), Ni (up to 800 ppm) and Cr_2O_5 (up to 1·5 wt %) and the presence of forsterite-rich olivine inclusions, suggesting that a rather primitive magma was involved in the formation of this rock. The felsic magma end-member appears to have been similar to the rhyodacite, because the compositions of quartz-hosted melt inclusions in the rhyodacite and the quartz-monzodiorite are virtually identical (Table 2). The felsic magma probably introduced the phenocrysts of quartz, anhydrite, apatite, Kfsp, titanite and biotite, whereas the mafic magma supplied the (now altered) phenocrysts of olivine and pyroxene. Hornblende, magnetite and plagioclase probably were introduced by both magmas.

In general, the rocks investigated during this study reveal a rather complex magma evolution that involved several stages of magma mixing. The compositional trends displayed by the melt inclusions are most easily explained by repeated intrusion of mafic magma into one (or several) magma chamber(s) of rhyodacitic to rhyolitic composition. Evidence for the presence of a relatively large magma chamber underneath the Hannover–Fierro pluton and the Santa Rita stock is found in the strong chemical similarity between these

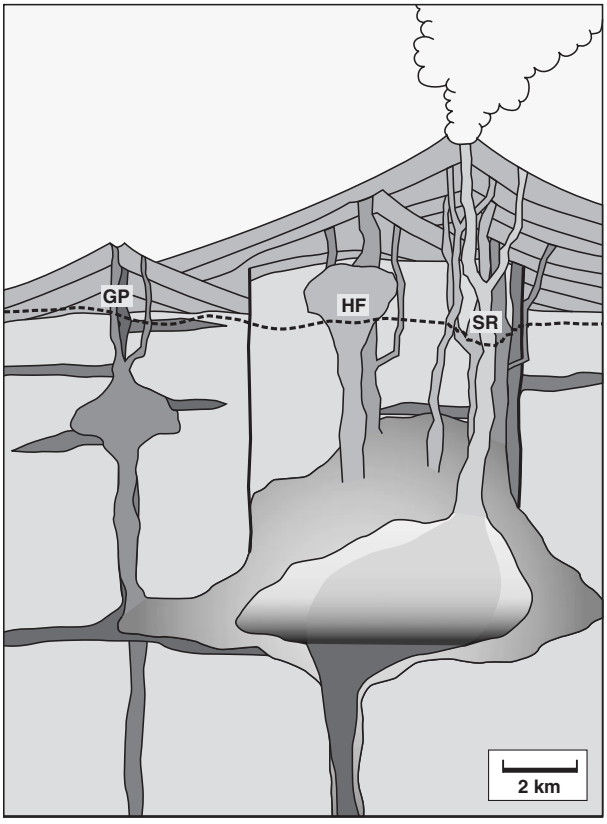

Fig. 10. Interpretative cross-section through the magmatic system at Santa Rita along line A–A′ marked in Fig. 2 (positions of magma chambers and eruption centers are hypothetical). The diagram shows a volcanic eruption triggered by intrusion of mafic magma (dark gray; on lower right) into an evolved, stratified magma chamber (light gray; above). The resulting hybrid andesite magma (medium gray) rises along a major conduit to the surface. GP, gabbro plug; HF, Hannover–Fierro pluton; SR, Santa Rita stock; dashed line marks present-day surface.

two intrusions (Jones *et al.*, 1967) and the spatial distribution of intermediate to felsic dikes in this area (Fig. 2). Figure 10 illustrates how this magma system originally may have appeared.

Similar models have been proposed for many active volcanoes above convergent plate boundaries (e.g. Gerlach & Grove, 1982; Pallister *et al.*, 1997; Matthews *et al.*, 1999*b*; Cole *et al.*, 2000). These studies have shown that interaction between mafic and felsic magmas is a very common phenomenon in such systems, and that the arrival of new batches of mafic magma at the base of magma chambers can be the direct cause of volcanic eruptions.

BEHAVIOR OF SULFUR AND CHALCOPHILE ELEMENTS

Controls on sulfur solubility in magmas

Sulfur dissolves in silicate melts either as S^{2-} or SO_4^{2-}, depending on the oxidation state of the magma. The transition from S^{2-} predominance to SO_4^{2-} predominance (at the 90% level) occurs between log f_{O_2} = NNO − 1 and NNO + 1·5, largely independent of melt composition, pressure and temperature (e.g. Matthews *et al.*, 1999*a*). The relationship between f_{O_2} and the molar ratio of SO_4^{2-}/S^{2-} is approximated by the following equation of Wallace & Carmichael (1994):

$$\log\left[\frac{X_{SO_4^{2-}}}{X_{S^{2-}}}\right] = (1{\cdot}02\Delta\mathrm{NNO}) - 0{\cdot}45. \qquad (1)$$

At very low or high SO_4^{2-}/S^{2-} ratios, however, an empirical equation described by Matthews *et al.* (1999*a*) seems to provide more accurate results. At a given pressure and temperature, sulfur solubility displays a minimum at around log f_{O_2} = NNO, and increases towards both lower and higher oxygen fugacities (Carroll & Rutherford, 1988). A sulfur-saturated magma normally contains sulfides at reducing conditions (i.e. f_{O_2} < NNO + 0·45) and anhydrite (in rare cases barite) at oxidizing conditions (i.e. f_{O_2} > NNO + 0·45). However, depending on the activities of FeO and CaO in the melt, sulfide saturation may be attained also above NNO + 0·45, or anhydrite saturation below this threshold. A magma that contains significant amounts of dissolved reduced S can reach sulfide saturation by one of the following mechanisms (Naldrett, 1989): (1) increasing melt S content; (2) decreasing temperature; (3) decreasing melt FeO content; (4) increasing f_{O_2} (if f_{O_2} < NNO). The last leads to a higher melt Fe^{3+}/Fe^{2+} ratio and, therefore, to a lower FeO content. If a magma becomes saturated in sulfide minerals and/or an immiscible sulfide melt (for simplicity we collectively will call them 'sulfides'), chalcophile elements such as Cu and Au strongly partition into these phases, leaving behind a silicate melt that is severely depleted in these elements. Towards the end of magma crystallization magmatic sulfides tend to become oxidized and release their metal content to magmatic–hydrothermal fluids (e.g. Candela & Holland, 1986; Candela, 1989, 1992). Based on this behavior it has been proposed that magmatic sulfides may promote the mineralization potential of evolving magma systems by acting as temporary storage medium for the ore metals, thus preventing them from being incorporated at trace-concentration levels within silicate and oxide minerals. A critical evaluation of this model is presented below.

Evolution of sulfur and copper at Santa Rita

A plot of Cu vs SiO_2 in the analyzed melt inclusions shows a clear trend of decreasing Cu concentration with increasing SiO_2 concentration (Fig. 11), in agreement with observations made on calc-alkaline volcanic systems worldwide (e.g. Keith *et al.*, 1997; Maughan *et al.*, 2002; Halter *et al.*, 2002*a*, 2005). The highest

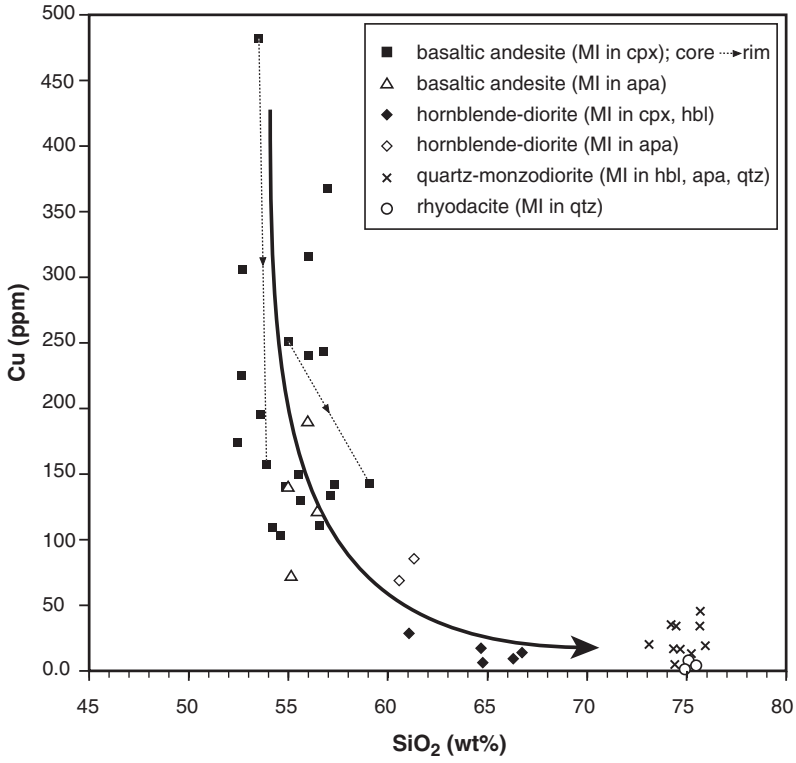

Fig. 11. Relationship between the Cu content and SiO_2 content of melt inclusions from Santa Rita. Noteworthy features are the general trend of decreasing Cu concentration with increasing SiO_2 concentration, and corresponding trends in individual augite phenocrysts (marked by dotted arrows).

Cu concentrations are observed in melt inclusions from the basaltic andesite (spanning a range from 100 ppm to nearly 500 ppm Cu), whereby the highest values represent melt inclusions analyzed in augite cores, and the lowest values melt inclusions analyzed in augite rims (Fig. 11; Table 2), implying that the Cu content of the silicate melt dropped over time. The presence of magmatic sulfide inclusions in some of these phenocrysts suggests that this decrease in melt Cu concentrations was caused by sulfide precipitation. The sulfide inclusions probably represent an immiscible sulfide melt, as their compositions plot in the liquid field of the Cu–Fe–S system at 1000–1050°C (Vaughan & Craig, 1997). Because the Cu content of this sulfide melt was very high (45 wt % Cu; see Table 3), small amounts of sulfide melt exsolution had a large impact on the Cu content of the remaining silicate melt.

Based on experimental data of Luhr (1990) and S contents of shoshonitic melt inclusions reported by Metrich & Clocciatti (1996), a S content of 0·1–0·2 wt % S is indicated for the basaltic andesite magma. This value represents a lower limit of the total S content of this magma because it does not incorporate any S bound in magmatic sulfides. It demonstrates, however, that the basaltic andesite magma was S-rich even if it did not carry significant amounts of magmatic sulfides.

The high abundance of sulfide inclusions in the hornblende-diorite porphyry most likely reflects the proposed magma mixing event. If the mafic magma end-member was similar to the basaltic andesite (i.e. 1000–1050°C; log f_{O_2} = NNO + 1; at sulfide saturation) and the felsic magma similar to the rhyodacite (i.e. 730–760°C; log f_{O_2} = NNO + 2·2; containing 1–3 vol. % anhydrite), admixture of rhyodacitic magma to the basaltic andesite magma simultaneously triggered three out of the four mechanisms leading to sulfide saturation: increased melt S content (as a result of dissolution of admixed anhydrite phenocrysts), decreased temperature, and decreased melt FeO content. Increasing f_{O_2} has counteracted this trend, but apparently was surpassed by the other effects. The resulting precipitation of magmatic sulfides caused the Cu content of the silicate melt to drop from several hundred ppm to less than 20 ppm (Table 2, Fig. 11). The two chemically distinct types of sulfide inclusion observed in the hornblendite xenolith (SR23) may represent a sulfide melt coexisting with pyrrhotite, provided that the liquid field present in the Cu–Fe–S system at 1000°C (Vaughan & Craig, 1997) extends

down to ~900°C in an analogous diagram for the composition of the type A inclusions. In such a case, the rather unusual partitioning behavior of Cu, which normally partitions into the sulfide liquid, could be explained.

The presence of 1–3 vol. % anhydrite phenocrysts in the rhyodacite implies a magmatic S content of 0·25–0·75 wt %. Although such a high value can theoretically be achieved by fractional crystallization of a S-rich precursor magma, it seems more plausible that S was added to the rhyodacitic magma by high-temperature fluids originating from the mafic magmas that repeatedly entered the Santa Rita magmatic system. Such a scenario, which includes the accumulation of sulfur-rich fluids in the upper part of the magma chamber, was invoked to explain the S-rich nature of magmas erupted at Mt. Pinatubo and Lascar Volcano (e.g. Hattori, 1993; Keppler, 1999; Matthews *et al.*, 1999*b*). Copper carried up by S-rich fluids originating from cooling mafic magmas may partly have been incorporated into (rare) sulfides in the overlying rhyodacite magma, providing an explanation for the presence of Cu-rich sulfides. At 730–760°C, both the Cu-rich and Cu-poor sulfide inclusions present in the rhyodacite were trapped as solids, the former as an intermediate solid solution, and the latter as pyrrhotite (Vaughan & Craig, 1997).

Comparison with other occurrences

The reconstructed evolution of S and chalcophile elements at Santa Rita is similar to that of other porphyry-Cu related systems such as Bingham or Alumbrera (Keith *et al.*, 1997; Hattori & Keith, 2001; Halter *et al.*, 2002*a*, 2004*a*; Maughan *et al.*, 2002), and is characteristic for S-rich volcanoes in general (e.g. Mt. Pinatubo—Pallister *et al.*, 1992, 1997; Hattori, 1993; DeHoog *et al.*, 2004; Lascar Volcano—Matthews *et al.*, 1999*b*; El Chichón—Luhr *et al.*, 1984; Nevado del Ruiz—Fournelle, 1990; Sigurdsson *et al.*, 1990). Mt. Pinatubo is of particular interest in this context, because the still active volcanic system has already developed associated porphyry-Cu mineralization (Hattori & Keith, 2001). In all occurrences, magmatic evolution is dominated by repeated injection of hot, mafic magma into a magma chamber of intermediate to felsic composition. The mafic input magmas are usually rather oxidized ($\log f_{O_2} \geq$ NNO + 1), relatively S-rich (≥0·1 wt % S) and contain no or only few sulfides, whereas the felsic magmas typically contain primary anhydrite and are saturated with an aqueous fluid phase. Intermediate magma types can often be proved to have formed by magma mixing, and they typically contain abundant magmatic sulfides (e.g. Pallister *et al.*, 1992; Maughan *et al.*, 2002; Halter *et al.*, 2004*a*).

Quantitative models

Two quantitative models for the behavior of Cu and S in evolving magma chambers will be developed and discussed on the basis of realistic examples from Santa Rita: (a) closed-system fractional crystallization; (b) magma mixing and subsequent crystallization. For both models, the following input parameters have to be known: (1) the solubility of S in the melt; (2) the average S content of the precipitating sulfides; (3) the starting Cu content of the melt; (4) the partition coefficient of Cu between sulfides and melt ($D_{Cu,\ sulfide/melt}$); (5) the bulk partition coefficient of Cu between melt and the other crystallizing phases ($D_{Cu\ bulk\ min/melt}$).

Closed-system fractional crystallization

The case of closed-system fractional crystallization is modeled on the basis of the basaltic andesite. For this magma the following parameters apply.

(1) The solubility of S in the melt is set to 0·15 wt % S, based on experimental data of Luhr (1990) and S contents of shoshonitic melt inclusions reported by Metrich & Clocciatti (1996), defining a range of 0·1–0·2 wt % S.

(2) The S content of the sulfides is set to 35·5 wt % S, based on the phase relations in the Cu–Fe–S system (Vaughan & Craig, 1997) and the data listed in Table 3.

(3) The starting concentration of Cu in the melt is set to 500 ppm, which corresponds to the highest value found in melt inclusions from the basaltic andesite.

(4) The partition coefficient of Cu between sulfides and silicate melt is set to $D_{Cu,sulfide/melt} = 1000$. This estimate is derived from several independent datasets. A partition coefficient of $D_{Cu,sulfide/melt} = 900$–$1300$ is indicated by the composition of petrographically early sulfide and silicate melt inclusions in sample SR26. Experimentally derived values in the system basalt–sulfide at 1245°C and 1 bar suggest a $D_{Cu,sulfide/melt}$ of 500–1300 (Ripley *et al.*, 2002), whereas distribution coefficients measured in sulfide-bearing mid-ocean ridge basalt (MORB) glasses span a range of $D_{Cu,sulfide/melt} = 900$–$1400$ (Francis, 1990; Peach *et al.*, 1990).

(5) The bulk mineral–melt partition coefficient of Cu is calculated at $D_{Cu,\ bulk\ min/melt} = 0{\cdot}068$, based on a phenocryst assemblage of 25 vol. % augite, 10 vol. % plagioclase, 4 vol. % olivine and 3 vol. % magnetite (Table 1) and corresponding crystal–melt partition coefficients listed in Table 7. The volumetric mineral proportions translate into a relative weight fraction of $X_{cpx} = 0{\cdot}60$, $X_{plag} = 0{\cdot}20$, $X_{ol} = 0{\cdot}10$ and $X_{mgt} = 0{\cdot}10$, such that $D_{Cu,\ bulk\ min/melt} = 0{\cdot}60\ D_{Cu,\ cpx/melt} + 0{\cdot}20\ D_{Cu,\ plag/melt} + 0{\cdot}10\ D_{Cu,\ ol/melt} + 0{\cdot}10\ D_{Cu,\ mgt/melt} = 0{\cdot}068$.

Using these input parameters the distribution of Cu in the basaltic magma after 30 wt % crystallization is

Table 7: Mineral–melt partition coefficients for copper

Mineral	*n*	Coex.*	$D_{Cu,\ min/melt}$			Source
			Min.	Max.	Av.	
clinopyroxene	12	×	0·011	0·070	0·030	this study
clinopyroxene	8	×	0·009	0·142	0·082	Halter *et al*. (2004*a*)
amphibole	6	×		<0·1		this study
amphibole	8	×	0·002	0·275	0·121	Halter *et al*. (2004*a*)
plagioclase	5		0·003	0·046	0·025	this study
plagioclase	54	×	0·003	0·164	0·031	Halter *et al*. (2004*a*)
magnetite	7		0·170	0·630	0·400	this study
olivine	2	×	0·020	0·071	0·046	this study
biotite	2		0·900	1·960	1·430	this study
apatite	7	×	0·025	0·026	0·026	this study

*A cross denotes that melt inclusions and hosts were analyzed within the same grain, whereas grains of equivalent age were used in the other cases.

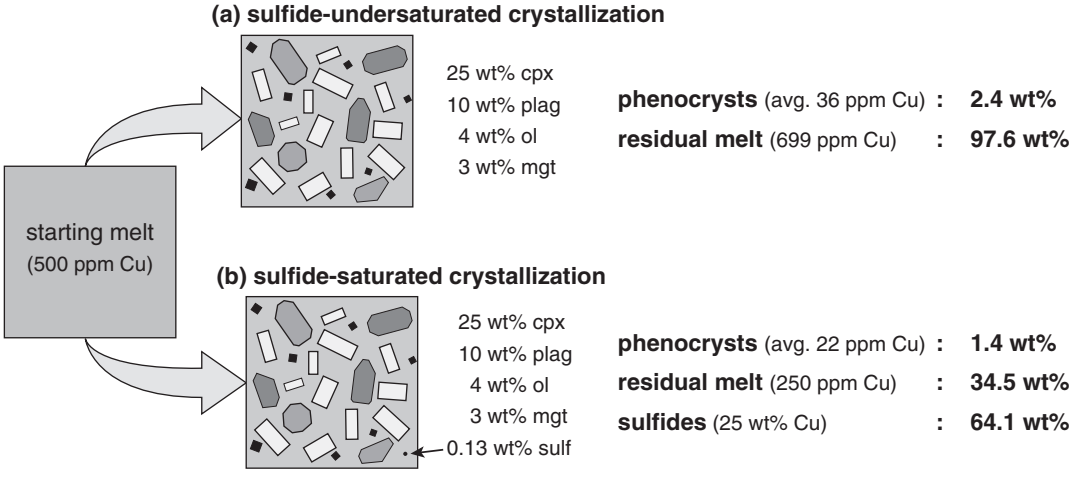

Fig. 12. Calculated distribution of Cu in the basaltic andesite after 30 wt % crystallization under (a) sulfide-undersaturated conditions, and (b) sulfide-saturated conditions. The percentage (by weight) of the total Cu in the system hosted by the individual phases is indicated by the bold numbers on the right.

calculated for the case of (a) sulfide-undersaturated, and (b) sulfide-saturated conditions (Fig. 12). For these calculations it is further assumed that: (1) no sulfides are present in the magma before crystallization begins; (2) the Cu content of already formed sulfides constantly re-equilibrates with the remaining silicate melt (as expected for sulfide liquids); (3) the Cu content of silicate and oxide minerals does not re-equilibrate (i.e. fractional crystallization).

The model predicts that after 30 wt % crystallization at sulfide-undersaturated conditions, 2·4 wt % of the total Cu in the system is incorporated in minerals. The remaining 97·6 wt % of the total Cu in the system is present in the residual silicate melt, which by then contains 699 ppm Cu. In the case of sulfide-saturated conditions, 63·7 wt % of the Cu resides in sulfides, 34·5 wt % in the residual silicate melt, and 1·4 wt % in the non-sulfide minerals at that stage. Although the presence of magmatic sulfides indeed leads to a reduction of the amount of Cu lost to other minerals (1·4 wt % vs 2·4 wt %), the amount of Cu ultimately available to fluids remains essentially the same (assuming subsolidus oxidation of the magmatic sulfides): it increases by only 1 wt % from 97·6 wt % to 98·6 wt % (Fig. 12). The model, therefore, suggests that magmatic sulfides do not significantly enhance the amount of Cu ultimately available for the ore-forming fluids, even if they are quantitatively resorbed towards

the end of magma solidification. Varying mineral proportions and other input parameters within geologically realistic limits does not affect this conclusion. Even in magmas with extremely high $D_{Cu,\ bulk\ min/melt}$ such as run *Jor46.10* of Barclay & Carmichael (2004), which contains 5·6 wt % cpx, 18·3 wt % hbl, 5·1 wt % biotite and 1·8 wt % spinel+apatite, less than 10 wt % of the total Cu will be incorporated in these minerals after 30 wt % crystallization.

Crystallization as a result of magma mixing

A major difference of magma mixing compared with closed-system fractional crystallization is that in the case of magma mixing the amount of precipitating sulfides is decoupled from the degree of crystallization. Sample SR27 from the hornblende-diorite porphyry will serve as an example to model this behavior. For the purpose of the calculation it is assumed that this rock was formed as a result of mixing between equal amounts of basaltic and rhyolitic melt similar to that preserved in the form of melt inclusions in the basaltic andesite and the rhyodacite. The S solubility in the mafic melt is assumed to be 0·15 wt % (as explained above), whereas a value of 0·005 wt % S was chosen for the rhyolite melt on the basis of microprobe analyses of rehomogenized melt inclusions in the rhyodacite and experimental data of Baker & Rutherford (1996). After mixing, the S solubility in the intermediate melt is estimated at 0·01 wt % S based on the experimental data of Carroll & Rutherford (1987). The mixing, therefore, causes exsolution of 0·068 wt % S (corresponding to 0·18 wt % sulfides) even before any crystallization takes place. The Cu concentration in the intermediate melt immediately after mixing is assumed to be 260 ppm, as expected from a 1:1 mixture of a basaltic melt containing 500 ppm Cu and a felsic melt containing 20 ppm Cu. The partition coefficient of Cu between sulfide and melt is set to $D_{Cu,sulfide/melt} = 1100$, based on the following observations: (1) LA-ICP-MS analyses of pyroxene-hosted sulfide and melt inclusions in sample SR27 indicate a $D_{Cu,sulfide/melt}$ of 800–1800; (2) experiments performed by Lynton *et al.* (1993) in the system rhyolite–pyrrhotite at 800°C and 1 kbar returned a $D_{Cu,\ pyrrhotite/melt}$ of 550 ± 220; (3) Jugo *et al.* (1999) determined a $D_{Cu,\ pyrrhotite/melt}$ of 2100–2900 in the system haplogranite–ISS (intermediate-solid-solution)–pyrrhotite at 850°C and 1 kbar. The reasons for the discrepancy between the experimental results of Lynton *et al.* (1993) and Jugo *et al.* (1999) are not clear. The bulk mineral–melt partition coefficient in the hornblende-diorite (25 vol. % plagioclase, 12 wt % hornblende, 4 wt % augite, 3 wt % magnetite) is calculated at 0·10. Magma evolution after the mixing event is modeled in two steps: (1) precipitation of 0·18 wt % sulfides; (2) crystallization of the phenocryst assemblage and concurrent precipitation of additional sulfides. All other parameters are the same as in the previous model.

The model predicts that after 30 wt % crystallization at sulfide-saturated conditions 82 wt % of the total Cu resides in the sulfides, 17 wt % in the residual melt (which by then contains 62 ppm Cu), and 1 wt % in the other minerals. If the same model is run without sulfides, 97 wt % of the total Cu resides in the melt, and 3 wt % in the minerals after 30 wt % crystallization. Hence, also in the case of magma mixing any temporary storage of ore metals in magmatic sulfides does not significantly enhance the amount of Cu ultimately available to magmatic–hydrothermal fluids (99% in the sulfide-bearing system vs 97% in the sulfide-free system).

DISCUSSION

The following lessons can be learnt from the quantitative models discussed above: (1) bulk non-sulfide mineral–melt partition coefficients of Cu are so low that only a small fraction of the total Cu is lost to silicate and oxide minerals; (2) in contrast to this, sulfide–melt partition coefficients are extremely high, such that in a sulfide-saturated magma the majority of the Cu is likely to be stored in the sulfides; (3) the presence or absence of magmatic sulfides has little influence on the amount of Cu available for the magmatic–hydrothermal fluids, provided that all magmatic sulfides are resorbed during the lifetime of the magmatic–hydrothermal system. If some magmatic sulfides are protected from later destruction (e.g. as a result of inclusion in phenocrysts), the amount of Cu available to the fluids will be reduced.

Evidence for temporary storage of the majority of chalcophile elements in magmatic sulfides and their subsequent destruction has recently been documented from the Farallón Negro Volcanic Complex in Argentina (Halter *et al.*, 2002*a*, 2005). It was found that the Cu/Au ratio of magmatic sulfides analyzed from pre-mineralization subvolcanic rocks closely matches the Cu/Au ratio of the bulk ore in the Alumbrera porphyry-Cu deposit, which is the largest ore body associated with this volcanic complex. Similar observations were made in the Bingham district, where S, Cu, Mo, and Pb were lost from slowly cooled regions of the Castro Gulch sill in the same proportions as that of the mineralization (Stavast *et al.*, in preparation). At Santa Rita, a rigorous comparison cannot be made at present because Mo/Cu/Au ratios are known only from a single sample (SR23; Table 3), and because the metal ratio of the entire mineralization is not well constrained. Mutschler *et al.* (1999) reported a Cu:Mo:Ag:Au-ratio of $1:(9{\cdot}2 \times 10^{-3}):(4{\cdot}8 \times 10^{-5}):(1{\cdot}8 \times 10^{-6})$ for the Central District (including the Hannover–Fierro Pluton), compared with

Cu:Mo:Ag:Au ratios of $\sim$1:(3×10^{-3}):(4×10^{-3}):(1×10^{-4}) and $\sim$1:($<1 \times 10^{-4}$):($<8 \times 10^{-5}$):($<1 \times 10^{-5}$), respectively, in the two sulfide types encountered in sample SR23.

The findings made in Alumbrera and Bingham suggest that virtually all Cu, Mo and Au was temporarily hosted by magmatic sulfides, and that no element fractionation occurred between magmatic sulfide formation and ore precipitation. This observation should not be taken as evidence, however, that the magmatic sulfides contributed to the overall metal enrichment process. The model calculations presented above imply that magmatic sulfides are not vital to the formation of porphyry-Cu deposits. The common presence of magmatic sulfides in porphyry-Cu related rocks is a consequence of the S-rich nature of the corresponding magmas, and the match between the metal ratios in the magmatic sulfides and those of the ore is simply a consequence of the fact that magmatic sulfides—if present—temporarily host nearly the entire budget of Cu, Mo, Au and Ag of the magma. As such, the pre-ore sulfide melt inclusions appear to be indicative of the ore metal ratios of the bulk ore of associated porphyry-type ore deposits, which could be highly relevant for exploration.

It is feasible, however, that magmatic sulfides exert a positive influence on the mineralization potential by holding back ore metals until favorable conditions for mineralization occur (see Halter *et al.*, 2005). In this model, porphyry-Cu mineralization occurs late in the evolution of a volcanic–plutonic system and is temporally not related to the arrival of new batches of mafic magma. Evidence from other porphyry-Cu systems such as Bingham Canyon or Mt. Pinatubo, on the other hand, suggests that these two processes, injection of basaltic magma and porphyry-type ore formation, are intimately linked with each other (Hattori & Keith, 2001). The question of whether magmatic sulfides can promote the mineralization potential by a mechanism other than the one treated in the quantitative models herein can, therefore, not fully be answered at present.

CONCLUSIONS

The magmatic evolution reconstructed for Santa Rita shares many similarities with that described from Mt. Pinatubo and other S-rich volcanoes situated above subduction zones (Mt. Pinatubo—Pallister *et al.*, 1992, 1997; Hattori, 1993; DeHoog *et al.*, 2004; Lascar Volcano—Matthews *et al.*, 1999*b*; El Chichón—Luhr *et al.*, 1984; Nevado del Ruiz—Fournelle, 1990; Sigurdsson *et al.*, 1990). In all these occurrences, magmatic evolution is dominated by repeated injection of hot, mafic magma into a comparatively cool, anhydrite-bearing magma of intermediate to felsic composition. The role of the mafic magmas is to supply Cu and additional S to the magma chamber, and to provide heat to retard solidification of the magma in the chamber, allowing for long-lived volcanic–plutonic activity (see also Hattori & Keith, 2001). The most primitive magma identified at Santa Rita is a K-rich basaltic andesite that equilibrated at 1000–1050°C, 1–3 kbar and $\log f_{O_2}$ = NNO + 0·7 to NNO + 1·0, whereas the felsic end-member is of rhyodacitic to rhyolitic composition and records crystallization conditions of 730–760°C and $\log f_{O_2}$ = NNO + 1·3 to NNO + 1·9. Mixing of mafic and felsic magma resulted in the precipitation of significant amounts of sulfides, as monitored by a drop in the Cu content of the silicate melt by one order of magnitude. Similar observations have been made in the porphyry-Cu systems at Bingham (Keith *et al.*, 1997; Hattori & Keith, 2001; Maughan *et al.*, 2002) and Alumbrera (Halter *et al.*, 2002*a*, 2004*a*, 2005). Characteristic for the mafic input magmas in both active and fossil volcanic systems is a high degree of alkalinity (often shoshonitic), a high oxidation state (mostly above NNO + 1), and a high S content (1000–5000 ppm).

A quantitative crystallization model based on LA-ICP-MS analyses of melt inclusions, sulfide inclusions and host minerals from Santa Rita was used to explore the effects of magmatic sulfides on the metal-enrichment process. The results suggest that intermittent stability of magmatic sulfides in crustal magma chambers does not significantly increase the amount of Cu ultimately available for magmatic–hydrothermal fluids, independent of whether the magma evolution is modeled as closed-system fractional crystallization or as a result of magma mixing. Whether magmatic sulfides promote the mineralization potential by preventing ore metals being lost during volcanic activity, however, remains a matter of debate.

ACKNOWLEDGEMENTS

We would like to express our gratitude to Thomas Wenzel and Michael Marks (both at Universität Tübingen) for carrying out the electron probe analyses and helping with the QUILF program, respectively. The manuscript significantly benefited from reviews by Jim Luhr, Jeff Keith and an anonymous reviewer, as well as from discussions with David Dolejs and Werner Halter.

REFERENCES

Andersen, D. J., Lindsley, D. H. & Davidson, P. M. (1993). QUILF: a PASCAL program to assess equilibria among Fe–Mg–Mn–Ti oxides, pyroxenes, olivine, and quartz. *Computers and Geosciences* **19**, 1333–1350.

Anderson, A. T. J. (1974). Evidence for a picritic, volatile-rich magma beneath Mt. Shasta, California. *Journal of Petrology* **15**, 243–267.

Anderson, J. L. (1996). Status of thermobarometry in granitic batholiths. *Transactions of the Royal Society of Edinburgh: Earth Sciences* **87**, 125–138.

Anderson, J. L. & Smith, D. R. (1995). The effects of temperature and f_{O_2} on the Al-in-hornblende barometer. *American Mineralogist* **80**, 549–559.

Audétat, A., Pettke, T. & Dolejs, D. (2004). Magmatic anhydrite and calcite in the ore-forming quartz-monzodiorite magma at Santa Rita, New Mexico (USA): genetic constraints on porphyry-Cu mineralization. *Lithos* **72**, 147–161.

Bacon, C. R. & Hirschmann, M. M. (1988). Mg/Mn partitioning test for equilibrium between coexisting Fe–Ti oxides. *American Mineralogist* **73**, 57–61.

Bacon, C. R., Newman, S. & Stolper, E. (1992). Water, CO_2, Cl, and F in melt inclusions in phenocrysts from three Holocene explosive eruptions, Crater Lake, Oregon. *American Mineralogist* **77**, 1021–1030.

Baker, L. L. & Rutherford, M. J. (1996). Crystallization of anhydrite-bearing magmas. *Transactions of the Royal Society of Edinburgh: Earth Sciences* **87**, 243–250.

Barclay, J. & Carmichael, I. S. E. (2004). A hornblende basalt from Western Mexico: water-saturated phase relations constrain a pressure-temperature window of eruptibility. *Journal of Petrology* **45**, 485–506.

Bodnar, R. J. (1995). Fluid inclusion evidence for a magmatic source of metals in porphyry copper deposits. In: Thompson, J. F. H. (ed.) *Magmas, Fluids and Ore Deposition. Mineralogical Association of Canada, Short Course Series*, **23**, 139–152.

Candela, P. A. (1989). Magmatic ore-forming fluids: thermodynamic and mass transfer calculations of metal concentrations. In: Whitney, J. A. & Naldrett, A. J. (eds) *Ore Deposition Associated with Magmas. Reviews in Economic Geology*, **4**, 203–221.

Candela, P. A. (1992). Controls on ore metal ratios in granite-related ore systems: an experimental and computational approach. *Transactions of the Royal Society of Edinburgh: Earth Sciences* **83**, 317–326.

Candela, P. A. & Holland, H. D. (1986). A mass transfer model for copper and molybdenum in magmatic hydrothermal systems: the origin of porphyry-type ore deposits. *Economic Geology* **81**, 1–19.

Carroll, M. R. & Rutherford M. J. (1987). The stability of igneous anhydrite: Experimental results and implications for sulfur behavior in the 1982 EI Chichon trachyandesite and other evolved magmas. *Journal of Petrology* **28**, 781–801.

Carroll, M. & Rutherford, M. J. (1988). Sulfur speciation in hydrous experimental glasses of varying oxidation state: results from measured wavelength shifts of sulfur x-rays. *American Mineralogist* **73**, 845–849.

Chou, I. M. (1987). Oxygen buffer and hydrogen sensor techniques at elevated pressures and temperatures. In: Ulmer, G. C. & Barnes, H. L. (eds) *Hydrothermal Experimental Techniques*.. Chichester: John Wiley, pp. 61–99.

Cole, J. W., Thordarson, T. & Burt, R. M. (2000). Magma origin and evolution of White Island (Whakaari) Volcano, Bay of Plenty, New Zealand. *Journal of Petrology* **41**, 867–895.

Danyushevsky, L. V., Della-Pasqua, F. N. & Sokolov, S. (2000). Re-equilibration of melt inclusions trapped by magnesian olivine phenocrysts from subduction-related magmatism: petrological implications. *Contributions to Mineralogy and Petrology* **138**, 68–83.

DeHoog, J. C. M., Hattori, K. H. & Hoblitt, R. P. (2004). Oxidized sulfur-rich mafic magma at Mount Pinatubo, Philippines. *Contributions to Mineralogy and Petrology* **146**, 750–761.

Evans, A. M. (1993). *Ore Geology and Industrial Minerals; an Introduction*. Oxford: Blackwell Science.

Evans, B. W. & Scaillet, B. (1997). The redox state of Pinatubo dacite and the ilmenite–hematite solvus. *American Mineralogist* **82**, 625–629.

Fournelle, J. H. (1990). Anhydrite in the Nevado del Ruiz November 1985 pumice: relevance to the sulfate problem. *Journal of Volcanology and Geothermal Research* **42**, 189–201.

Francis, R. D. (1990). Sulfide globules in mid-ocean ridge basalts (MORB) and the effect of oxygen abundance in Fe–S–O liquids on the ability on those liquids to partition metals from MORB and komatiitic magmas. *Chemical Geology* **85**, 199–213.

Gaetani, G. A. & Watson, E. B. (2002). Modeling the major-element evolution of olivine-hosted melt inclusions. *Chemical Geology* **183**, 25–41.

Gerlach, D. C. & Grove, T. L. (1982). Petrology of Medicine Lake Highland volcanics: characterization of endmembers of magma mixing. *Contributions to Mineralogy and Petrology* **80**, 147–159.

Ghiorso, M. S. & Sack, R. O. (1991). Fe–Ti oxide geothermometry: thermodynamic formulation and the estimation of intensive variables in silicic magmas. *Contributions to Mineralogy and Petrology* **108**, 485–510.

Günther, D., Audétat, A., Frischknecht, R. & Heinrich, C. A. (1998). Quantitative analysis of major, minor and trace elements in fluid inclusions using laser ablation-inductively coupled plasma-mass spectrometry (LA-ICP-MS). *Journal of Analytical Atomic Spectrometry* **13**, 263–270.

Halter, W. E., Pettke, T. & Heinrich, C. A. (2002*a*). The origin of Cu/Au-ratios in porphyry-type ore deposits. *Science* **296**, 1844–1846.

Halter, W. E., Pettke, T., Heinrich, C. A. & Roth-Rutishauser, B. (2002*b*). Major to trace element analysis of melt inclusions by laser-ablation ICP-MS: methods of quantification. *Chemical Geology* **183**, 63–86.

Halter, W. E., Heinrich, C. A. & Pettke, T. (2004*a*). Laser-ablation ICP-MS analysis of silicate and sulfide melt inclusions in an andesitic complex II: evidence for magma mixing and magma chamber evolution. *Contributions to Mineralogy and Petrology* **147**, 397–412.

Halter, W. E., Pettke, T. & Heinrich, C. A. (2004*b*). Laser-ablation ICP-MS analysis of silicate melt and sulfide melt inclusions in an andesitic complex I: analytical approach and data evaluation. *Contributions to Mineralogy and Petrology* **147**, 385–396.

Halter, W. E., Heinrich, C. A. & Pettke, T. (2005). Magma evolution and the formation of porphyry Cu–Au ore fluids: evidence from silicate and sulfide melt inclusions. *Mineralium Deposita* **39**, 845–863.

Harrison, T. M. & Watson, E. B. (1984). The behavior of apatite during crustal anatexis: equilibrium and kinetic considerations. *Geochimica et Cosmochimica Acta* **48**, 1467–1477.

Hattori, K. (1993). High-sulfur magma, a product of fluid discharge from underlying mafic magma: evidence from Mount Pinatubo, Philippines. *Geology* **21**, 1083–1086.

Hattori, K. H. & Keith, J. D. (2001). Contribution of mafic melt to porphyry copper mineralization: evidence from Mount Pinatubo, Philippines, and Bingham Canyon, Utah, USA. *Mineralium Deposita* **36**, 799–806.

Hedenquist, J. W. & Lowenstern, J. B. (1994). The role of magmas in the formation of hydrothermal ore deposits. *Nature* **370**, 519–527.

Heinrich, C. A., Pettke, T., Halter, W., Aigner-Torres, M., Audétat, A., Günther, D., Hattendorf, B., Bleiner, D., Guillong, M. & Horn, I. (2003). Quantitative multi-element analysis of minerals, fluid and melt inclusions by laser-ablation inductively-coupled-plasma mass-spectrometry. *Geochimica et Cosmochimica Acta* **67**, 3473–3496.

Hernon, R. M., Jones, W. R. & Moore, S. L. (1964). *Geology of the Santa Rita Quadrangle, New Mexico. US Geological Survey, Map* **GQ 306**.

Holland, T. & Blundy, J. (1994). Non-ideal interactions in calcic amphiboles and their bearing on amphibole–plagioclase thermometry. *Contributions to Mineralogy and Petrology* **116**, 433–447.

Johnson, M. C. & Rutherford, M. J. (1989). Experimentally determined conditions in the Fish Canyon Tuff, Colorado, magma chamber. *Journal of Petrology* **30**, 711–737.

Jones, W. R., Hernon, R. M. & Moore, S. L. (1967). *General Geology of the Santa Rita Quadrangle, Grant Country, New Mexico. US Geological Survey Professional Papers* **555**.

Jugo, P. J., Candela, P. A. & Piccoli, P. M. (1999). Magmatic sulfides and Au:Cu ratios in porphyry deposits: an experimental study of copper and gold partitioning at 850°C, 100 MPa in a haplogranite melt–pyrrhotite–intermediate solid solution–gold metal assemblage, at gas saturation. *Lithos* **46**, 573–589.

Keith, J. D., Whitney, J. A., Hattori, K., Ballantyne, G. H., Christiansen, E. H., Barr, D. L., Cannan, T. M. & Hook, C. J. (1997). The role of magmatic sulfides and mafic alkaline magmas in the Bingham and Tintic mining districts, Utah. *Journal of Petrology* **38**, 1679–1690.

Kelemen, P. B. & Hanghøj, K. (2004). One view of the geochemistry of subduction-related magmatic arcs, with an emphasis on primitive andesite and lower crust. In: Rudnick, R. L. (ed.) *Treatise on Geochemistry—The Crust*. Elsevier: Oxford, pp. 593–659.

Keppler, H. (1999). Experimental evidence for the source of excess sulfur in explosive volcanic systems. *Science* **284**, 1652–1654.

Lattard, D., Sauerzapf, U. & Käsemann, M. (2005). New calibration data for the Fe–Ti oxide thermo-oxybarometers from experiments in the Fe–Ti–O system at 1 bar, 1000–1300°C and a large range of oxygen fugacities. *Contributions to Mineralogy and Petrology* **149**, 735–754.

Leake, B. E., Woolley, A. R. & Arps, C. E. S., *et al.* (1997). Nomenclature of amphiboles: report of the subcommittee on amphiboles of the international mineralogical association, commission on new minerals and mineral names. *Canadian Mineralogist* **35**, 219–246.

Lindsley, D. H. & Frost, B. R. (1992). Equilibria among Fe–Ti oxides, pyroxenes, olivine, and quartz: Part I. Theory. *American Mineralogist* **77**, 987–1003.

Longerich, H. P., Jackson, S. E. & Günther, D. (1996). Laser ablation inductively coupled plasma mass spectrometric transient signal data acquisition and analyte concentration calculation. *Journal of Analytical Atomic Spectrometry* **11**, 899–904.

Lowenstern, J. B. (1995). Application of silicate–melt inclusions to the study of magmatic volatiles. In: Thompson, J. F. H. (ed.) *Magmas, Fluids and Ore Deposition. Mineralogical Association of Canada, Short Course Series* **23**, 71–98.

Lowenstern, J. B. & Mahood, G. A. (1991). New data on magmatic H_2O contents of pantellerites, with implications for petrogenesis and eruptive dynamics at Pantelleria. *Bulletin of Volcanology* **54**, 78–83.

Lu, F., Anderson, A. T. & Davis, A. M. (2005). Diffusional gradients at the crystal/melt interface and their effects on the composition of melt inclusions. *Journal of Geology* **103**, 591–597.

Luhr, J. F. (1990). Experimental phase relations of water- and sulfur-saturated arc magmas and the 1982 eruptions of El Chichón volcano. *Journal of Petrology* **31**, 1071–1114.

Luhr, J. F., Carmichael, I. S. E. & Varekamp, J. C. (1984). The 1982 eruptions of El Chichón Volcano, Chiapas, Mexico: mineralogy and petrology of the anhydrite-bearing pumices. *Journal of Volcanology and Geothermal Research* **23**, 69–108.

Lynton, S. J., Candela, P. A. & Piccoli, P. M. (1993). An experimental study of the partitioning of copper between pyrrhotite and a high-silica rhyolitic melt. *Economic Geology* **88**, 901–915.

Matthews, S. J., Moncrieff, D. H. S. & Carroll, M. R. (1999*a*). Empirical calibration of the sulfur valence oxygen barometer from natural and experimental glasses: method and applications. *Mineralogical Magazine* **63**, 421–431.

Matthews, S. J., Sparks, R. S. J. & Gardeweg, M. C. (1999*b*). The Piedras Grandes–Soncor eruptions, Lascar Volcano, Chile; evolution of a zoned magma chamber in the Central Andean upper crust. *Journal of Petrology* **40**, 1891–1919.

Maughan, D. T., Keith, J. D., Christiansen, E. H., Pulsipher, T., Hattori, K. & Evans, N. J. (2002). Contributions from mafic alkaline magmas to the Bingham porphyry Cu–Au–Mo deposit, Utah, USA. *Mineralium Deposita* **37**, 14–37.

Metrich, N. & Clocciatti, R. (1996). Sulfur abundance and its speciation in oxidized alkaline melts. *Geochimica et Cosmochimica Acta* **60**, 4145–4160.

Moore, G. & Carmichael, I. S. E. (1998). The hydrous phase equilibria (to 3 kbar) of an andesite and basaltic andesite from western Mexico: constraints on water content and conditions of phenocryst growth. *Contributions to Mineralogy and Petrology* **130**, 304–319.

Mutschler, F. E., Ludington, S. & Bookstrom, A. A. (1999). Giant porphyry-related metal camps of the world—a database. *US Geological Survey Open-File Report* **99-556**. Online Version 1.0, available at: http://geopubs.wr.usgs.gov/open-file/of99-556/ (accessed January 2006).

Naldrett, A. J. (1989). Sulfide melts—crystallization temperatures, solubilities in silicate melts, and Fe, Ni, and Cu partitioning between basaltic magmas and olivine. In: Whitney, J. A. & Naldrett, A. J. (eds) *Ore Deposition Associated with Magmas. Reviews in Economic Geology* **4**, 5–20.

Pallister, J. S., Hoblitt, R. P. & Reyes, A. G. (1992). A basalt trigger for the 1991 eruptions of Pinatubo volcano? *Nature* **356**, 426–428.

Pallister, J. S., Hoblitt, R. P., Meeker, G. P., Knight, R. J. & Siems, D. F. (1997). Magma mixing at Mount Pinatubo: petrographic and chemical evidence from the 1991 deposits. In: Newhall, C. G. & Punongbayan, R. S. (eds) *Fire and Mud: Eruptions and Lahars of the Mount Pinatubo, Philippines*. Seattle, WA: University of Washington Press, pp. 687–731.

Parat, F., Dungan, M. & Streck, M. J. (2002). Anhydrite, pyrrhotite and sulfur-rich apatite: tracing the sulfur evolution of an Oligocene andesite (Eagle Mountain, CO, USA). *Lithos* **64**, 63–75.

Peach, C. L., Mathez, E. A. & Keays, R. R. (1990). Sulfide melt–silicate melt distribution coefficients for noble metals and other chalcophile elements as deduced from MORB: implications for partial melting. *Geochimica et Cosmochimica Acta* **54**, 3379–3389.

Perchuk, L. L., Aranovich, L. Y., Podlesskii, K. K., Lavrant'eva, I. V., Gerasimov, V. Y., Fed'kin, V. V., Kitsul, V. K., Karaskov, L. P. & Berdnikov, N. V. (1985). Precambrian granulites of the Aldan shield, eastern Siberia, USSR. *Journal of Metamorphic Petrology* **3**, 265–310.

Pettke, T., Halter, W. E., Webster, J. D., Aigner-Torres, M. & Heinrich, C. A. (2004). Accurate quantification of melt inclusion chemistry by LA-ICPMS: a comparison with EMP and SIMS and advantages and possible limitations of these methods. *Lithos* **78**, 333–361.

Rickwood, P. C. (1989). Boundary lines within petrologic diagrams which use oxides of major and minor elements. *Lithos* **22**, 247–263.

Ripley, E. M., Brophy, J. G. & Li, C. (2002). Copper solubility in a basaltic melt and sulfide liquid/silicate melt partition coefficients of Cu and Fe. *Geochimica et Cosmochimica Acta* **66**, 2791–2800.

Rose, A. W. & Baltosser, W. W. (1966). The porphyry copper deposit at Santa Rita, New Mexico. In: Titley, S. R. & Hicks, C. L. (eds) *Geology of the Porphyry Copper Deposits in Southwestern North America.*. Tucson, AZ: University of Arizona, pp. 205–220.

Scaillet, B. & Evans, B. W. (1999). The 15 June 1991 eruption of Mount Pinatubo. I. Phase equilibria and pre-eruption P – T – f_{O_2}–f_{H_2O} conditions of the dacite magma. *Journal of Petrology* **40**, 381–411.

Sigurdsson, H., Carey, S., Palais, J. M. & Devine, J. (1990). Pre-eruption compositional gradients and mixing of andesite and dacite magma erupted from Nevado del Ruiz Volcano, Colombia in 1985. *Journal of Volcanology and Geothermal Research* **41**, 127–151.

Stavast, W. J. A., Keith, J. D., Christiansen, E. H., Dorais, M. J., Tingey, D., Larocque, A. & Evans, N. (2006). The fate of magmatic sulfides during intrusion or eruption, Bingham and Tintic Districts, Utah. *Economic Geology* **101**, 329–345.

Thomas, J. B., Bodnar, R. J., Shimizu, N. & Chesner, C. A. (2003). Melt inclusions in zircon. In: Hanchar, J. M. & Hoskin, P. W. O. (eds) *Zircon. Mineralogical Society of America, Reviews in Mineralogy*, **53**, 63–87.

Titley, S. R. (1993). Characteristics of porphyry copper occurrence in the American Southwest. In: Kirkham, R. V., Sinclair, W. D., Thorpe, R. I. & Duke, J. M. (eds) *Mineral Deposit Modeling. Geological Association of Canada, Special Papers*, **40**, 433–464.

Titley, S. R. & Anthony, E. Y. (1989). Laramide mineral deposits in Arizona. In: Jenney, J. P. & Reynolds, S. J. (eds) *Geologic Evolution of Arizona. Arizona Geological Society Digest* **17**, 485–514.

Vaughan, D. J. & Craig, J. R. (1997). Sulfide ore mineral stabilities, morphologies, and intergrowth textures. In: Barnes, H. L. (ed.) *Geochemistry of Hydrothermal Ore Deposits*. Chichester: John Wiley and Sons, pp. 367–434.

Wallace, P. J. & Carmichael, I. S. E. (1994). S speciation in submarine basaltic glasses as determined by measurements of SKα X-ray wavelength shifts. *American Mineralogist* **79**, 161–167.

Watson, B. E. & Harrison, M. T. (1983). Zircon saturation revisited: temperature and composition effects in a variety of crystal magma types. *Earth and Planetary Science Letters* **64**, 295–304.

APPENDIX

Melt inclusion quantification

Quantification of LA-ICP-MS analyses of melt inclusions was performed according to the method described by Halter *et al.* (2002*a*, 2004*b*) and Pettke *et al.* (2004). In this method, the mass fraction of ablated host vs inclusion is arithmetically varied until the calculated melt composition matches a predefined geochemical criterion. If the analyzed melt inclusions originate from a magma system that follows a well-defined geochemical trend, such criteria can be defined on the basis of whole-rock analyses by assuming that the compositions of the melt inclusions lie on the same trend as that displayed by the whole-rocks. Successful application of this technique requires that the analyzed melt inclusions and whole-rocks are truly consanguineous, and that both the melt inclusions and the whole-rocks are not significantly affected by alteration. A major source of uncertainty on the melt inclusion compositions stems from the signal deconvolution into contributions from ablated host and ablated inclusion [illustrated by Pettke *et al.* (2004)]. Obviously, this uncertainty increases with increasing chemical similarity between inclusion and host, being small for chemically simple host minerals such as quartz and apatite, but becoming important for chemically complex host minerals such as clinopyroxene and hornblende.

Here we used geochemical trends displayed by 24 whole-rock analyses published by Jones *et al.* (1967) to define the mass fraction of ablated host vs inclusion required for melt inclusion quantification. Although many of these rocks are not fresh, the elements used for quantification are considered to have remained immobile because alteration is dominantly of propylitic nature. The occurrence of apatite-hosted melt inclusions in different magma types at Santa Rita allows independent checking of the results because most major elements (except for CaO and P_2O_5) can be determined with high accuracy. By exploring different geochemical criteria and comparing the results obtained for inclusions hosted by different minerals, two important prerequisites for a successful signal deconvolution have been identified: (1) the elements selected as 'internal standards' should have rather dissimilar mineral–melt partition coefficients; (2) their absolute concentrations in the melt

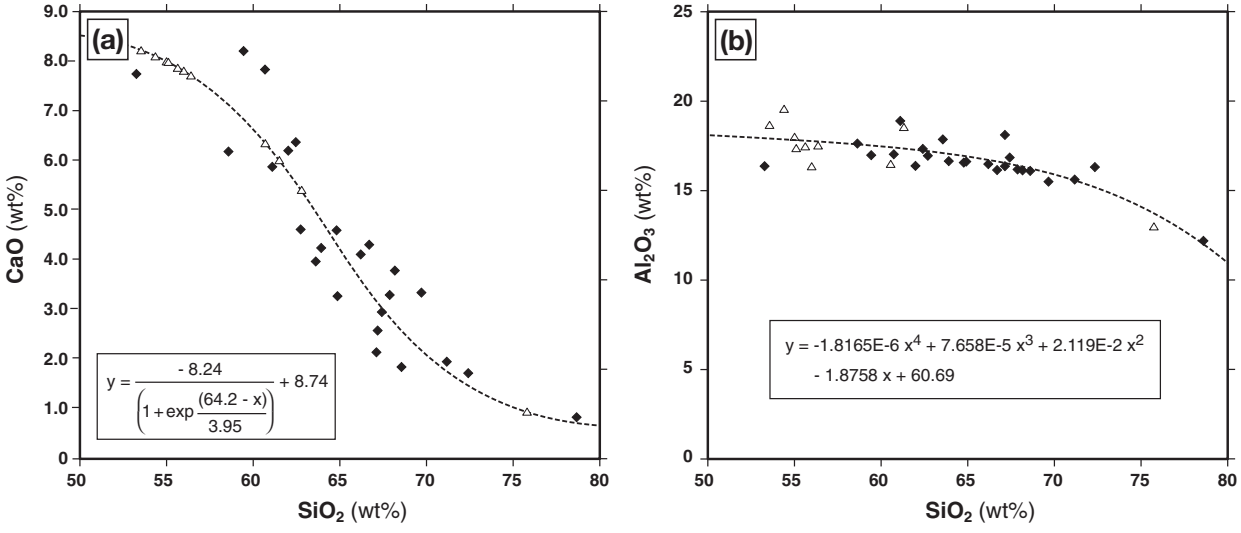

should be high. The best results for apatite-hosted melt inclusions were obtained with the CaO–SiO_2 relationship (Fig. A1a), whereas the Al_2O_3–SiO_2 relationship (Fig. A1b) proved most suitable for all other host minerals. Calculated Al_2O_3 and SiO_2 contents of apatite-hosted inclusions fit well onto the Al_2O_3–SiO_2 trend displayed by the whole-rocks, thus validating the assumption of consanguinity.

Do melt inclusions represent true aliquots of the surrounding melt?

It has been demonstrated convincingly that boundary-layer phenomena do not affect melt inclusions greater than 25 μm in diameter (e.g. Anderson, 1974; Lowenstern & Mahood, 1991; Bacon *et al.*, 1992; Thomas *et al.*, 2003; Lu *et al.*, 2005), hence we are confident that the analyzed inclusions originally contained true aliquots of the surrounding melt. However, melt inclusion compositions can change in response to diffusional re-equilibration and post-entrapment crystallization of material along the inclusion walls, as documented for Mg and Fe in olivine-hosted melt inclusions (e.g. Danyushevsky *et al.*, 2000; Gaetani & Watson, 2002). Post-entrapment crystallization along the inclusion walls does not represent a problem for LA-ICP-MS analysis as long as large enough pit sizes are used (Halter *et al.*, 2002*b*; Pettke *et al.*, 2004), because any material precipitated along the walls is removed during ablation and reassigned to the inclusion during quantification. Diffusional re-equilibration, on the other hand, indeed may have affected certain elements with high intercrystalline diffusivities, such as Na in the quartz-hosted melt inclusions.